Probing light-matter interactions in atomically thin 2D material

By

Jonghwan Kim

A dissertation submitted in partial satisfaction of the

requirements for the degree of

Doctor of Philosophy

in

Physics

in the

Graduate Division

of the

University of California, Berkeley

Committee in charge:

Professor Feng Wang, Chair

Professor Michael F. Crommie

Professor Xiang Zhang

Spring 2015

Abstract

Understanding light-matter interactions in atomically thin 2D material

by

Jonghwan Kim

Doctor of Philosophy in Physics

University of California, Berkeley

Professor Feng Wang, Chair

Recently, atomically thin 2D materials have emerged as a new class of nanomaterial with extraordinary physical properties ranging from semi-metal (graphene), semiconductors (transition metal dichalcogenides) to insulators (hBN). Due to its unusual linear electronic spectrum, graphene has been studied as a platform where exotic quantum mechanical phenomena take place and electro-optical property can be greatly tuned by electrostatic gating. On the other hand, in semiconducting transition metal dichalcogenides (TMD), many body particles such as exciton and trion can be readily accessed even at room temperature due to strong Coulomb interaction. There are further exciting opportunities in heterostructures where layer-layer interaction provides new physics and functionalities. In this thesis, I explore light-matter interaction in 2D materials and their heterostructure with laser spectroscopy techniques.

First of all, I study electromagnetic interaction between graphene and optical cavity via Rayleigh scattering spectroscopy. Although light-matter interaction in graphene is extremely strong for atomically thin thickness, overall optical response in macroscopic scale is still limited. Combination of graphene and resonant cavity can amplify the interaction dramatically. Therefore, it is important to understand the electromagnetic interaction between two systems. In this study, I find that the coupling can be explained by real and imaginary part of graphene dielectric constant which affects cavity resonance frequency and quality factor, respectively. In addition to

fundamental interest, it also shows that this platform has promising potential for novel sensing application and electro-optical modulator.

Secondly, I study valley-selective dipole interaction of exciton states in a monolayer transition metal dichalcogenides. Due to crystal symmetry, an extra degree of freedom, valley state, is available in this system. In analogy to spin state, it is important to understand and manipulate valley state with light. In this study, I demonstrate that valley excitonic states in a monolayer WSe2 can be manipulated by femtosecond pulse with the control of polarization. Ultrafast pump-probe spectroscopy shows that circularly-polarized femtosecond pulse induces valley-selective optical Stark effect which acts as a pseudomagnetic field. This demonstrates efficient and ultrafast control of the valley excitons with optical light, and opens up the possibility to coherent manipulate the valley polarization for quantum information applications.

Lastly, I study interlayer interaction in heterostructure of MoS2/WS2 where strong exciton binding energy plays an important role. Simple band theory predicts that a heterostructure of two different semiconducting TMD layers forms type-II heterostructure. However, it is not clear how strong Coulomb interaction plays a role in terms of charge transfer dynamics. In this study, I demonstrate ultrafast charge transfer in MoS2/WS2 via both photoluminescence mapping and femtosecond (fs) pump-probe spectroscopy. Despite large exciton binding energy, hole transfer from the MoS_2 layer to the WS_2 layer takes place within 50 fs after optical excitation. Such ultrafast charge transfer in van der Waals heterostructures indicates that it can enable novel 2D devices for optoelectronics and light harvesting.

Contents

LIST OF FIGURES…….. iii

ACKNOWLEDGEMENTS…….. iv

CHAPTER 1 – INTRODUCTION…….. 1

1.1 MOTIVATION AND BACKGROUND…… 1
1.2 GRAPHENE…… 2
1.2.1 Electronic band structure……... 2
1.2.2 Optical property…….. 3
1.3 A MONOLAYER MX2…….. 5
1.3.1 Electronic band structure…….. 5
1.3.2 Strong coulomb interaction……... 6
1.3.3 Valley degree of freedom……... 7
1.4 THESIS HIGHLIGHTS…… 8

CHAPTER 2 – ELECTRICAL CONTROL OF OPTICAL PLASMON RESONANCE WITH GRAPHENE MOTIVATION AND BACKGROUND

2.1 INTRODUCTION…….. 10
2.1.1 Tunable interband transition in graphene……... 11
2.2 EXPERIMENT……... 13
2.2.1 Optical spectrum measurement……. 13
2.2.2 Sample preparation…… 13
2.3 RESULT AND DISCUSSION…… 15
2.3.1 Effect of graphene…… 15
2.3.2 Cavity modulation with electrostatic gating……. 16
2.3.3 Numerical simulation and possibility as a bio/chemical sensing……. 20
2.4 COMPARISON TO HYBRID STRUCTURE WITH PHOTONIC CRYSTAL CAVITY…… 21
2.4.1 Photonic crystal cavity……. 22
2.4.2 Effect of graphene on high Q cavity……... 23
2.4.3 Possibility as a fast electro-optic modulator…….. 23
2.5 CONCLUSION……. 25

CHAPTER 3 – ULTRAFAST GENERATION OF PSEUDOMAGNETIC FIELD FOR VALLEY EXCITONS IN WSE2 MONOLAYERS……... 26

3.1 INTRODUCTION…… 26
3.1.1. Optical Stark effect…….. 27

3.1.2. Valley-selective dipole interaction in MX2……. 28
3.2 EXPERIMENT……. 29
3.2.1 Photoluminescence and linear absorption measurement…. 29
3.2.2 Transient absorption spectrum measurement (Pump-probe spectroscopy)……. 29
3.2.3 CVD-grown monolayer WSe2 sample…… 30
3.3 RESULT AND DISCUSSION……. 31
3.3.1 Optical transition in a monolayer WSe2…… 31
3.3.2 Circular polarization dependent photoluminescence…… 32
3.3.3 Valley-selective optical Stark effect……. 33
3.3.4 Control of energy shift with pump power and detuning…... 37
3.3.5 Estimation of pseudomagnetic field magnitude……. 38
3.4 CONCLUSION AND OUTLOOK…….. 39

CHAPTER 4 – ULTRAFAST CHARGE TRANSFER IN MOS2/WS2 HETEROSTRUCTURE……. 40

4.1 INTRODUCTION……. 40
4.2 EXPERIMENT…….. 42
4.2.1 Photoluminescence and Raman spectroscopy…… 43
4.2.2 (Transient) Absorption spectroscopy…….. 43
4.2.3 Heterostructure preparation…… 43
4.3 RESULT AND DISCUSSION……. 43
4.3.1 Optical micrograph of sample and Raman spectra…….. 43
4.3.2 Photoluminescence spectrum and mapping of heterostructure…… 44
4.3.3 Transient absorption measurement……... 46
4.3.4 Determination of charge transfer time…….. 49
4.3.5 Effect of Coulomb interaction and lattice mismatch on charge transfer dynamics……. 51
4.4 CONCLUSIONS AND OUTLOOK…… 52
BIBLIOGRAPHY…..……...54

List of Figures

Figure 1.1 Lattice structure of graphene…… 2

Figure 1.2 Band structure of graphene by tight binding model…… 3

Figure 1.3 Illustration of tunable interband transition in graphene…… 4

Figure 1.4 Lattice structure of a monolayer MX2……. 5

Figure 1.5 Band structure of a monolayer MX2 near K and K' points……... 6

Figure 2.1 Gate-dependent complex dielectric constant of graphene…….. 13

Figure 2.2 SEM image of a gold nanorod…… 14

Figure 2.3 Effect of graphene on the gold nanorod plasmon resonance…….. 16

Figure 2.4 Electrical control of the plasmon resonance……. 18

Figure 2.5 Comparison between experiment and theory…… 19

Figure 2.6 Numerical simulation result…… 21

Figure 2.7 Scanning electron micrograph (SEM) of the fabricated cavities with graphene…… 22

Figure 2.8 Effect of graphene on high Q cavity…… 23

Figure 3.1 Illustration of optical Stark effect…… 28

Figure 3.2 Optical micrograph of a monolayer WSe2 on sapphire substrate…… 31

Figure 3.3 Absorption spectra of a monolayer WSe2…….. 32

Figure 3.4 Circular polarization dependent photoluminescence spectra……... 33

Figure 3.5 Valley-dependent optical Stark effect with non-resonant circularly polarized pump……... 34

Figure 3.6 Time evolution and spectral lineshape of the valley-dependent transient reflection spectra for σ_+ pump and σ_+ probe configuration…… 36

Figure 3.7 Pump detuning and pump intensity dependence of the valley-selective optical Stark shift…38

Figure 4.1 Band alignment and structure of MoS_2/WS_2 heterostructures……..41

Figure 4.2 Schematic of heterostructure and Raman spectra……..44

Figure 4.3 Photoluminescence (PL) spectra and mapping of MoS_2/WS_2 heterostructures at 77 K……. 45

Figure 4.4 Transient absorption spectra of MoS_2/WS_2 heterostructures……48

Figure 4.5 Ultrafast hole transfer dynamics from vertical cuts in Figure 4.4a and 4.4b…….....50

Acknowledgment

It is difficult to find words to sufficiently express my gratitude to my advisor, Prof. Feng Wang. I was extremely lucky to meet him during the exchange program 8 years ago. I dreamed to become a physicist after I observed high standard and exciting research in his group as an undergraduate intern. During PhD program under his guidance, I could obtain numerous valuable academic assets for my future career such as presentation skill with clarity and critical reasoning with good understanding on physics.

I am also grateful to Prof. Yuen-Ron Shen. In addition to his endless enthusiasm and extraordinary excellence in physics, I observed a pathway to great science from his successful students and post-docs.

I could not ask for better colleagues than the students and postdoctoral fellows in Wang group. Not only being good physicists, they are also great as human being which made me enjoy 5 years as a graduate student. Dr. David J. Cho, Dr. Steven Byrnes and Dr. Tsung-Ta Tang helped to get my own research started in my first year. Also, as senior fellows with tough duties, they taught me how to become a responsible lab member. Dr. Arka Majumdar showed me different aspects of research from engineering side. While working and having a discussion with him, I started to think about what is an important and interesting problem to myself instead of chasing what other people like. I am truly indebted to Dr. Xiaoping Hong for many things. He thought me various skills in ultrafast optics and software to perform desired experiment in the most accurate and efficient ways. Working with him, I observed great successes thanks to his optimism and persistence which shaped my attitude to scientific research. Without him, it is hard to imagine how I could grow up as who

I am now. Dr. Sufei Shi showed how to communicate with people outside the group in the professional manner. He generously gave an advice for academic career which help to plan my own. Also, his expertise in electrical transport was invaluable for my projects. I was very lucky to meet Chenhao Jin. He is probably one of the smartest I have ever met among my ages. He is not only brilliant in fundamental physics but also obtains experimental data with high standard. I especially appreciate for his theoretical support on projects. I would like to thank Steve Drapcho for his help on developing techniques for 2D heterostructures. The technique enabled many interesting projects. My thanks also goes to other members, past and present, Long Ju, Jason Horng, Bo Zeng, Halleh B. Balch, Yaqing Bie, Dr. Zhiwen Shi, Dr. Jihun Kang, Lili Jiang, Dr. Huiling Han, Dr. Yinghui Sun, Dr. Yu-Chieh Wen, Dr. Kaihui Liu, Dr. Baisong Geng, Hyungmok Son, Jingying Yue and Matthew Kam.

I am also grateful to colleagues outside Wang group. Prof. Junqiao Wu, Dr. Sefaattin Tongay, Joonki Suh provided high quality crystals and nano fabrication. Prof. Yanfeng Zhang and Yu Zhang provided CVD-grown MoS2 and WS2 samples. Prof. Lance Li, Chih-Yuan S. Chang, and Ming-Hui Chiu provided CVD-grown WSe2 samples. Also, I would like to thank Prof. Mike Crommie and Prof. Xiang Zhang for their advice and encouragement as thesis co-advisers.

Finally and most importantly, I want to thank my parents and my sister for their love, care and belief in me for the past thirty years. My father himself taught me science and mathematics when I was young which made me begin to enjoy science. My mother supported me both emotionally and physically. I rely on my sister many things for my family while I am far apart from Korea. Without them, my life would never be pleasant and fulfilling. This thesis is dedicated to them.

Chapter 1. Introduction

1.1 Motivation and background

An atomically thin two-dimensional structure had known to be thermodynamically unstable so that it cannot exist in nature. It has been only a decade when free-standing 2D materials are isolated from layered materials. Layered materials has strong in-plane covalent bonding whereas it has weak out-of-plane van-der-Waals bonding. Thus, they can be cleaved layer by layer. Geim and Novoselov discovered that these materials can be actually thinned down to a monolayer by micromechanical exfoliation method. They demonstrated that a monolayer of graphite, MoS2 and other layered materials can be obtained in the laboratory[1].

Isolation of such monolayers was big enough surprise, but shortly people discovered exciting new possibilities of these new materials in terms of fundamental physics and novel device applications. Different layered materials have distinct electronic properties such as a superconductor, metal, semi-metal, semiconductor and insulator. It is unexplored and interesting questions how two dimensionality affect such electronic properties. Furthermore, there is even bigger opportunities by combining different monolayers to form a heterostructure[2].

My research focuses on understanding optical properties of such atomically thin 2D materials and heterostructures for novel optoelectronics applications. In this chapter, I will introduce electronic band structure and optical properties of 2D materials, graphene and a monolayer MX2, which are of main focus in my study.

1.2 Graphene

1.2.1 Electronic band structure

Graphene is a two-dimensional single atomic layer of carbon atoms. It has a hexagonal lattice structure with two equivalent carbon atoms as sublattice. It forms like a Honeycomb structure as shown in Figure 1.1. Carbon atoms form SP^2 bonding. Important electrical and optical properties arise from extra p_z orbitals of a carbon atom. Electronic band structure can be calculated by tight binding model with the nearest neighbor couplings of this p_z orbital[3].

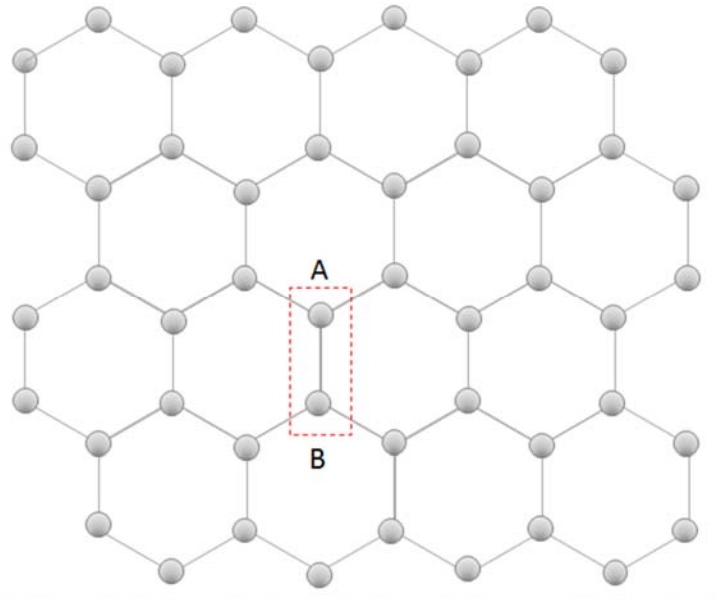

Figure 1.1 Lattice structure of graphene Dashed box denotes sublattice sites A and B where two identical carbon atoms locate.

Band structure shows that conduction and valence bands are meeting at two single points, so called Dirac point, at K and K' point. At Dirac point, it possesses a conical electronic structure where band dispersion is linear. Due to such a unique linear dispersion, a low-energy electron in graphene behaves like a massless particle and thus its motion should be described by Dirac

equation rather than Schrodinger equation[1]. For this reason, graphene is a tabletop platform where theory for quantum electrodynamics can be tested. As a result, it has attracted an enormous interest and effort to understand its fundamental behavior of charge carrier in graphene.

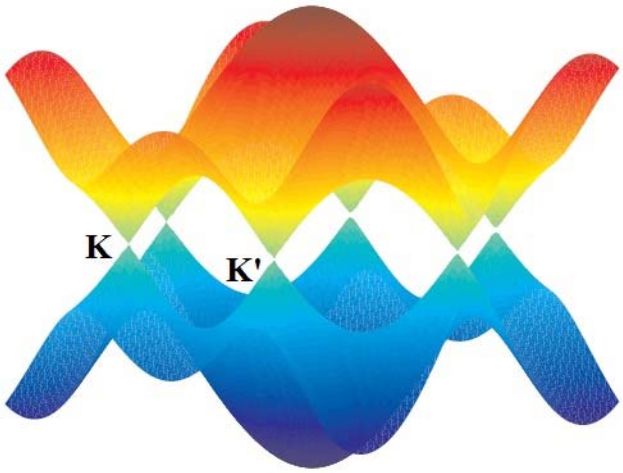

Figure 1.2 Band structure of graphene by tight binding model Conduction band and valence band meet at single points at K and K' points in momentum space. Band dispersion is linear near Dirac points.

1.2.2 Optical property

Besides fascinating electrical properties, graphene has unique and interesting optical properties. Despite its single atomic thickness, light-matter interaction in graphene is extremely strong. Pristine graphene absorbs light at optical frequency by 2.3 percent which is twenty times stronger than absorption coefficient of GaAs at band edge for the same thickness[4]. Furthermore, absorption covers broad spectrum ranging from the far infrared to the ultraviolet. What is even more interesting is that strong and broadband optical response can be tuned by electrostatic doping.

Light absorption in graphene originates from two different contributions: intraband transition and interband transition. Depending on the spectral frequency, one optical transition is

relatively more important than the other. At optical frequency, interband transition play a dominant role than intraband transition from free carrier[5]. Absorption spectrum of pristine graphene due to interband transition is frequency independent, and it is determined by the fine-structure constant, πα. Interband transition in graphene can be modified dramatically with electrostatic doping. This is because density of state near Dirac point is small so that Fermi level can be tuned by significant energy difference. As a result, optical transition can be turned on and off by Pauli blocking (Figure 1.3)[4]. In chapter 5, more detailed will be discussed.

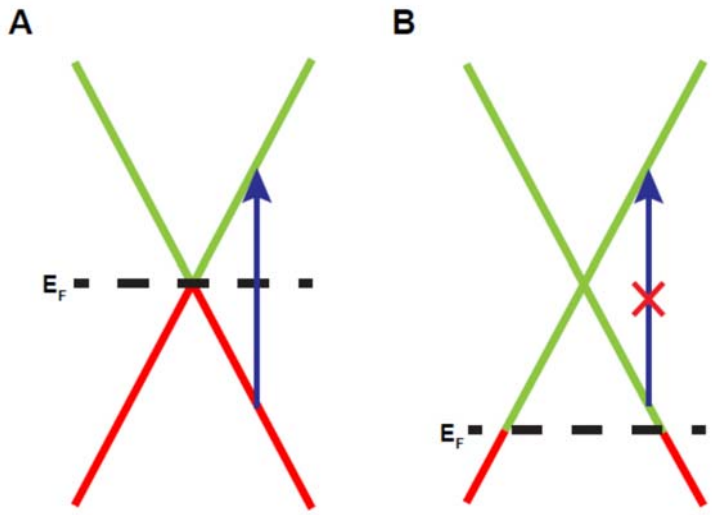

Figure 1.3 Illustration of tunable interband transition in graphene A and B show band structure of graphene where Fermi level is tuned by electrostatic doping. Compared to pristine graphene (A) where Fermi level locates at Dirac point, highly doped graphene (B) has significantly lowered (hole doping) or raised (electron doping) Fermi level. As a result, optical transition (blue arrow) can be blocked due to Pauli blocking.

1.3 A monolayer MX2

1.3.1 Electronic band structure

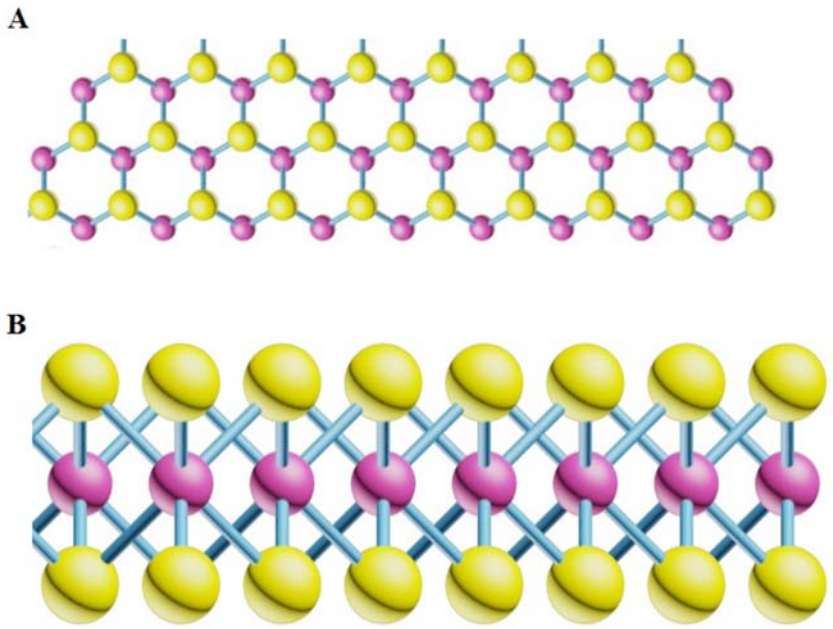

Figure 1.4 Lattice structure of a monolayer MX2 A. (Top view) Magenta atom corresponds to transition metal atom and yellow atom corresponds to chalcogen atom. B. (Side view) Three layered structure of unit layer MX2.

A monolayer MX2 also has a honeycomb lattice structure. In this system, d-electron orbitals plays important roles[6, 7]. In comparison to graphene, main difference of interest is broken inversion symmetry in sublattice sites. Site 'A' has a transition metal atom (Mo and W), and site 'B' has two chalcogen atoms (S and Se) as shown in Figure 1.4. Different combination of transition metal atom and chalcogen atom show qualitatively similar behavior. Such explicitly broken inversion symmetry makes electronic structure of monolayer MX2 distinct from graphene.

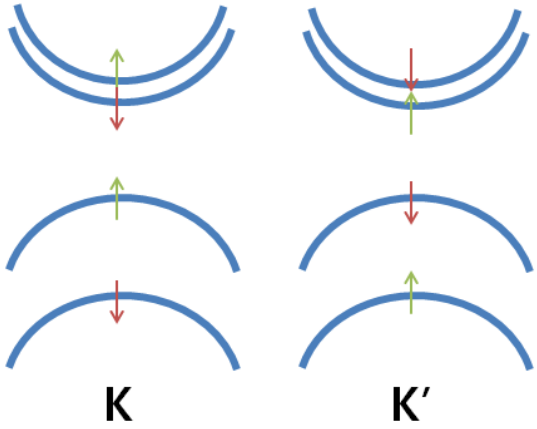

Figure 1.5 Band structure of a monolayer MX2 near K and K' points Green and red arrows represent a spin state of bands.

Figure 1.5 shows electronic band structure of a monolayer MX2[8]. First of all, instead of a pair of Dirac cone with zero band gap, it has a pair of degenerate direct band gap at K and K' point. Zero band gap in graphene originates from inversion symmetry in two sublattice sites. In this sense, finite band gap in a monolayer MX2 can be understood by the broken symmetry. Especially, band gap locates at visible frequency which makes this system favorable to various optoelectronic applications. In addition, broken inversion symmetry provides other unique advantages for spintronics and valleytronics in this system. I will discuss on this shortly below.

1.3.2 Strong coulomb interaction

Although band theory with symmetry consideration can predicts an electronic band structure, a simple one particle theory is not enough to describe real optical properties of this system. One needs to consider strong Coulomb interaction among charge carriers[9-11]. Especially, such effect becomes dramatic in low dimensional system as screening of electric field between quasiparticles is suppressed significantly. As a result, exciton in a monolayer MX2 has large

binding energy according to 2D hydrogenic model (eq. 1.1). Experimentally, such large binding energy (> 0.5 eV) is confirmed by different techniques such as reflection contrast measurement, two-photon absorption measurement and scanning tunneling microscopy. Large exciton binding energy in this system is an important issue to understand physical properties in a heterostructure which will be discussed in Chapter 4.

$$E_b^n = \frac{\mu e^4}{2\hbar^2\varepsilon^2(n-1/2)^2} \qquad \textbf{(eq. 1.1)}$$

μ: ***reduced mass of exciton,*** ε: ***effective dielectric constant,*** **n**: ***Exciton quantum number***

1.3.3 Valley degree of freedom

In general, a valley state refers to degenerate local electronic band structure in momentum space arising from crystal symmetry. Well-known example is Si which as diamond-like lattice structure. It has multiple degenerate points in momentum space, and they can be controlled by strain. However, valley state in Si is difficult to control[12]. On the other hand, a monolayer MX2 have valley states at their band gap and it is relatively easier to control[8]. From hexagonal lattice symmetry, it has two degenerate direct bandgap at K and K' point in momentum space. Due to explicitly broken inversion symmetry, spin states split its degeneracy and couple to so-called valley states. Although inversion symmetry is broken, time reversal symmetry is not broken. With such condition, eq. 1.2 shows that a spin state at two different valleys cannot have the same energy. Together with strong spin-orbit coupling from a transition metal atom, spin states at each valley splits with large energy in an opposite way as shown in Figure 1.5. This is particularly useful for potential spintronics/valleytronics applications as spin and valley relaxation time can be potentially slow. This is because flipping spin index alone is forbidden by the valley-contrasting spin splitting.

$$\textbf{Time reversal symmetry: } E^{\uparrow}(k) = E^{\downarrow}(-k) \qquad \textbf{(eq. 1.2)}$$

Broken inversion symmetry: $\boldsymbol{E^{\uparrow}(k) \neq E^{\uparrow}(-k)}$

Third, optical selection rules at two valleys depends on circular polarization of incident light. This is because of valley-contrasting dipole interaction matrix element against circular polarization excitation. I will discuss on this more detailed in Chapter 3. Valley selective dipole interaction provides powerful control for valley and spin states in this system.

1.4 Thesis highlights

In the following chapters, I will show my work on understanding optical properties of graphene and a monolayer MX2.

In Chapter 2, I demonstrate that optical resonances in a gold nanorod and photonic crystal cavity can be efficiently modulated by graphene where Fermi level is tuned by electrostatic doping. Exploiting the uniquely strong[13, 14] and gate-tunable interband transitions[4, 15] of graphene, I could achieve significant modulation of both the resonance frequency and quality factor of the resonantor. For a god nanorod case, our analysis shows that the plasmon-graphene coupling is remarkably strong: even a single electron in graphene at the plasmonic hotspot could have an observable effect on plasmon scattering intensity. Such hybrid graphene-nanometallic structure provides a powerful way for electrical control of plasmon resonances at optical frequencies, and could enable novel plasmonic sensing down to single charge transfer events. On the other hand, a graphene-photonic crystal device can potentially be useful for a high speed, and low power absorptive and refractive modulator, while maintaining a small physical footprint.

In Chapter 3, I demonstrate that an ultrafast and ultrahigh valley pseudo-magnetic field can be generated using circularly polarized femtosecond pulses to selectively control the valley degree of freedom in monolayer MX_2. Employing ultrafast pump-probe spectroscopy, I observed a pure and valley-selective optical Stark effect in WSe_2 monolayers from the non-resonant pump, which instantaneously lift the degeneracy of valley exciton transitions without any dissipation. The strength of the optical Stark effect scales linearly with both the pump intensity and the inverse of pump detuning. An energy splitting more than 10 meV between the K and K' valley transitions can be achieved, which corresponds to an effective pseudo-magnetic field over 60 Tesla. This study demonstrates efficient and ultrafast control of the valley excitons with optical light, and opens up the possibility to coherent manipulate the valley polarization for quantum information applications.

In Chapter 4, I show the experimental observation of ultrafast charge transfer in photo-excited MoS_2/WS_2 heterostructures using both photoluminescence mapping and femtosecond (fs) pump-probe spectroscopy. I find that hole transfer from the MoS_2 layer to the WS_2 layer takes place within 50 fs after optical excitation, a remarkable rate for van der Waals coupled 2D layers. Such ultrafast charge transfer in van der Waals heterostructures can enable novel 2D devices for optoelectronics and light harvesting.

Chapter. 2 Electrical control of optical plasmon resonance with graphene

2.1 Introduction

Surface plasmon resonance in nanoscale metal structures has attracted tremendous interest due to its unique capability to concentrate light into deep subwavelength scale[16]. In applications ranging from nano-antenna[17] to metamaterials[18, 19] it is often desirable to have plasmonic resonances that can be controlled in-situ with electrostatic gating. So far, such active plasmonic devices have been demonstrated only at terahertz frequencies employing hybrid semiconductor-metal nanostructures[20-22], because gate-induced free electrons in typical semiconductors have large response only at this low frequency range[23]. At optical frequencies (including near-infrared to visible), electrical control of plasmon resonance has been an outstanding challenge due to the dramatically reduced free electron responses with increasing frequency. Graphene, a novel zero-bandgap semiconductor[24, 25], provides a unique opportunity to address this challenge, because not only the low frequency free carrier response, but also high frequency interband transition in graphene can be conveniently varied through electrical gating[4, 15]. In addition, graphene can be readily integrated into the nanometer-sized hot spot in the nanometallic structure due to its single atom thickness and excellent compatibility with nanofabrication [26-28].

In this chapter, I demonstrate electrical controlled plasmonic resonance at near infrared using the hybrid graphene-gold nanorod structure as a model system. This is in contrast to intrinsic

graphene plasmonics that arises from free carriers at terahertz and far-infrared frequencies[29-31]. Such plasmon resonance control is also distinctly different from enhancing absorption for graphene photo detectors[32, 33]. I show that although graphene is only a single atom thick, its effect on the gold nanorod plasmon is remarkably strong: Electrical gating of graphene efficiently modulate all aspects of the plasmon resonance, including a 20 meV shift of resonance frequency, a 30% increase in quality factor, and a 30% increase in resonance scattering intensity. The plasmon resonance frequency shift and the resonance quality factor increase can be attributed to, respectively, changes in the real ($\varepsilon_g^{'}$) and imaginary ($\varepsilon_g^{''}$) part of the graphene dielectric constant upon electrical gating. Numerical analysis further shows that surprisingly few graphene electrons at the plasmon hot spots contribute to a large fraction of the plasmon modulation, with each additional electron changing the plasmon scattering intensity by about one thousandth. This intensity change is well within the detection limit of modern photonic technology, and it could enable ultrasensitive optical detection of single charge transfer events. The hybrid graphene-nanometallic structure therefore opens up opportunities not only to active control near-infrared plasmon resonances, but also to novel single-electron sensing.

Lastly, I will further discuss on a hybrid structure of graphene and dielectric cavity (photonic crystal (PhC) cavity) as a comparison to a metallic case. Optical resonance modulation with a PhC cavity shows significantly larger modulation depth due to low cavity loss. Possible application as an electro-optic modulator for optical interconnect will be discussed.

2.1.1 Tunable interband transition in graphene

Modulation of cavity resonance with an active medium can be described by change in complex dielectric constants. Gate-dependent complex dielectric constant of graphene has been

established previously in the literature[14, 34, 35]. The imaginary part $\varepsilon_g^{"}$ is characterized by a constant absorption of $\frac{\pi e^2}{\hbar c}$ above $2|E_F|$ from interband transitions and Drude absorption from free carriers (i.e. intraband transitions). The real part $\varepsilon_g^{'}$ can be obtained from $\varepsilon_g^{"}$ using the Kramer-Kronig relation. Specifically, energy-dependent $\varepsilon_g^{'}$ and $\varepsilon_g^{"}$ have the form[14, 34, 35]

$$\varepsilon'_g(E) = 1 + \frac{e^2}{8\pi E\varepsilon_0 d}\ln\frac{(E+2|E_F|)^2+\Gamma^2}{(E-2|E_F|)^2+\Gamma^2} - \frac{e^2}{\pi\varepsilon_0 d}\frac{|E_F|}{E^2+(1/\tau)^2} \qquad \text{(Eq. 2.1)}$$

$$\varepsilon"_g(E) = \frac{e^2}{4E\varepsilon_0 d}\left[1+\frac{1}{\pi}\left\{\tan^{-1}\frac{E-2|E_F|}{\Gamma} - \tan^{-1}\frac{E+2|E_F|}{\Gamma}\right\}\right] + \frac{e^2}{\pi\tau E\varepsilon_0 d}\frac{|E_F|}{E^2+(1/\tau)^2}$$

Here d is the thickness of graphene. The interband transition broadening Γ is estimated to be 110 meV from the graphene reflection spectrum. The free carrier scattering rate $1/\tau$ can be set to zero because it has little effect on the dielectric constants, $\varepsilon_g^{'}(E_R)$ and $\varepsilon_g^{"}(E_R)$, at the plasmon resonance energy E_R. The equations show that $\varepsilon_g^{"}(E_R)$ experiences a step like decrease when $2|E_F|$ is larger than E_R and blocks the relevant interband transitions. However, $\varepsilon_g^{'}(E_R)$ has a maximum at $2|E_F| = E_R$. This is because all optical transitions below E_R contribute a negative susceptibility, and transitions above E_R contribute a positive susceptibility to $\varepsilon_g^{'}(E_R)$.

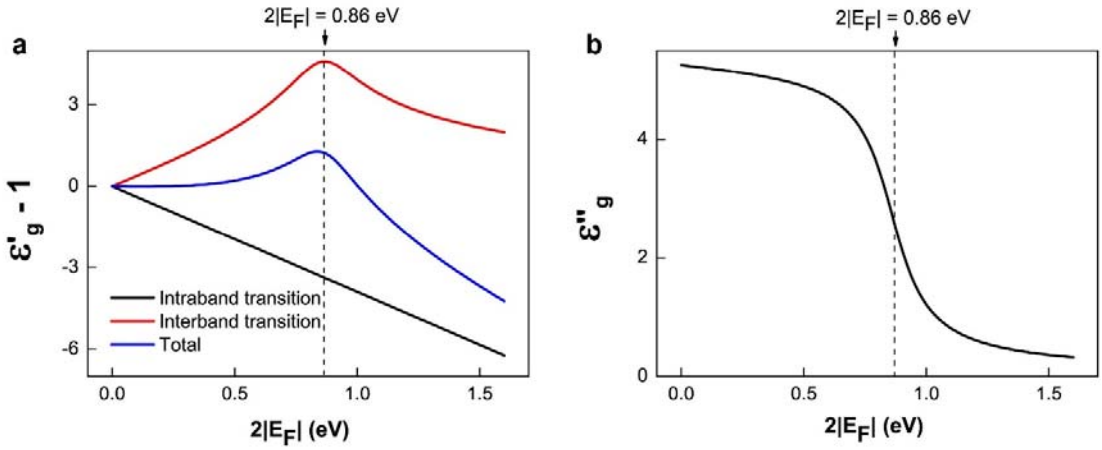

Figure 2.1 Gate-dependent complex dielectric constant of graphene Real (a) and imaginary part (b) of dielectric constant calculated for E = 0.86 eV which is at telecom frequency of interest in this work.

2.2 Experiment

2.2.1 Optical spectrum measurement

The plasmon resonance in a gold nanorod is probed using a dark-field Rayleigh scattering spectroscopy of an individual gold nanorod. On the other hand, the photonic crystal cavities are characterized in cross-polarized reflectivity measurement set-up where the cavity is kept at a 45 degree to an incident light polarization. Two measurement technique shares a common scheme which eliminates large background light not coupled to a cavity. For incident illumination, I used a supercontinuum laser as the broadband light source producing high brightness photons from 0.67 to 2.7 eV. The supercontinuum light is focused to excite an optical cavity in a microscopy setup. The light collected is analyzed by a spectrometer equipped with an InGaAs array detector.

2.2.2 Sample preparation

Chemical synthesized gold nanorods were purchased from Nanopartz (part number: 30-HAR-1400). The gold nanorods have a mean diameter of 25 nm and length of 200 nm, with a plasmon resonance energy at 860 meV[36]. Gold nanorods were deposited on a glass or SiO_2/Si substrate by spin coating at a spinning speed of 500 rpm. The substrate with gold nanorods was then immersed in acetone at 70 ℃ for 30 minutes to dissolve residual cetrimonium bromide (CTAB). On top of the nanorods we transferred a large-area graphene grown by chemical vapor deposition using the standard growth and transfer processes[37, 38]. Figure 2.2 displays a typical high-resolution scanning electron micrograph (SEM) of the gold nanorod covered by graphene on SiO_2/ Si substrate. Our SEM images show that the gold nanorods have a length distribution from 155 to 311 nm, and they form mostly well-separated individual rods in our devices. Transferred large area graphene draped nicely around the gold nanorods, as can be seen at the nanorod edges in the SEM image.

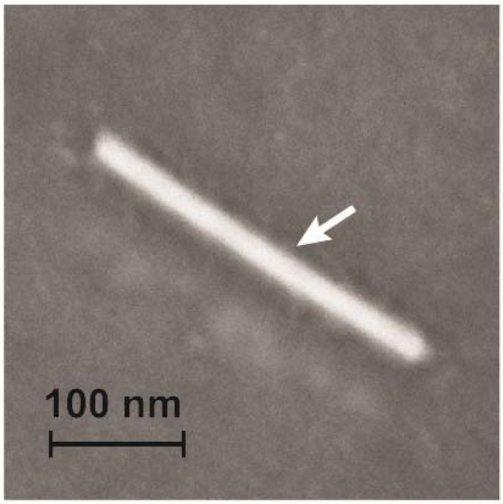

Figure 2.2 SEM image of a gold nanorod A typical high-resolution scanning electron micrograph (SEM) of the single gold nanorod covered by graphene. Individual gold nanorods are well-separated from each other in our devices, and graphene is observed to drape nicely over the nanorods (white arrow).

2.3 Result and discussion

2.3.1 Effect of graphene

Figure 2.3a and 2.3b display two representative single-particle Rayleigh scattering spectra of an ungated graphene-nanorod hybrid structure and a bare gold nanorod, respectively. Both scattering spectra exhibit prominent plasmon resonances at 0.86 eV (i.e. at the telecom wavelength of 1.5 μm). However, the plasmon resonance of the graphene-nanorod hybrid structure is much broader, with a full-width-half-maximum (FWHM) at 93 meV (compared to 70 meV in a bare gold nanorod). It is quite surprising that a monolayer thick graphene can lead to such large change in plasmon resonances in the gold nanorod. This underlines remarkably strong interband optical absorption of graphene at in optical frequencies (Figure 2.3c)[13, 14], which provides an efficient dissipation channel and increases the damping rate of the surface plasmon oscillation[26, 39].

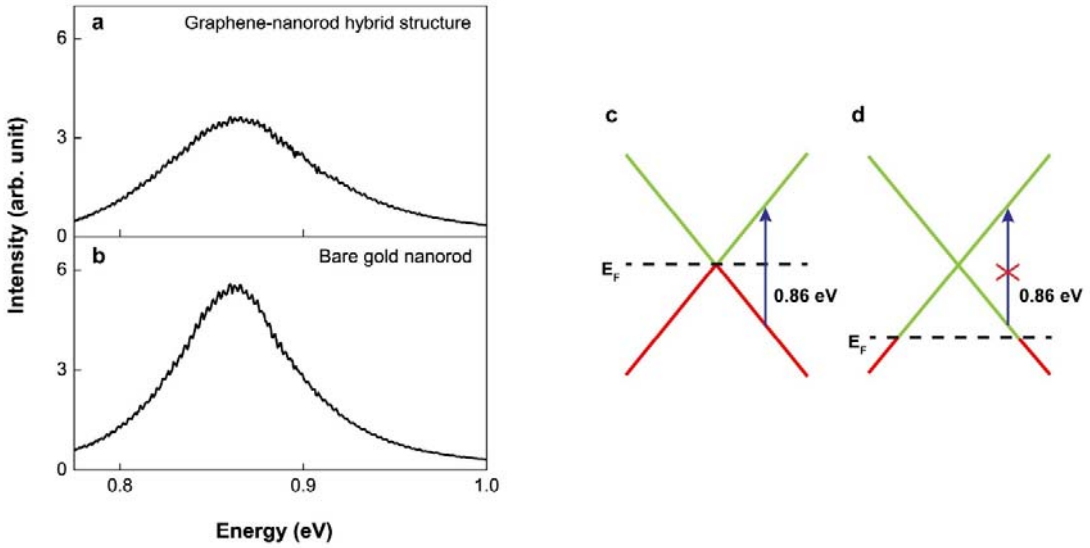

Figure 2.3 Effect of graphene on the gold nanorod plasmon resonance. a. Rayleigh scattering spectra of an as-prepared graphene-nanorod hybrid structure. **b**. Rayleigh scattering spectrum of a bare gold nanorod. Both scattering spectra exhibit prominent plasmon resonances at 0.86 eV (i.e. at the telecom wavelength of 1.5 μm), but the resonance

in graphene-nanorod hybrid structure is significantly broader due to extra dissipation channel from graphene absorption. **c**. Illustration of strong interband optical transitions present at all energies in pristine graphene. They contribute to the plasmon dissipation at 0.86 eV. **d**. Illustration showing that gate-induced shift in Fermi energy (E_F) can block the interband transition in graphene and reduce optical dissipation at 0.86 eV.

2.3.2 Cavity modulation with electrostatic gating

To modulate the plasmon resonance, one can simply eliminate the energy dissipation in graphene by switching off its interband optical transitions. This can be achieved through electrostatic gating: gated graphene has a shifted Fermi energy $|E_F|$, and optical transitions with energy less than $2|E_F|$ become forbidden due to empty initial states (or filled final states) for hole (or electron) doping (Figure 2.3d)[4, 15]. We can determine this gate-induced change in graphene absorption using infrared reflection spectroscopy. Figure 2.4a displays the gate-induced reflectivity change δR/R at the plasmon resonance energy 0.86 eV in an area with only graphene. It shows a step-function-like decrease in reflectivity, corresponding to reduced graphene absorption[14], at large hole doping (with V_g lower than -0.1 V). This gate-dependent reflectivity curve indicates that our as-prepared graphene under ionic liquid is strongly hole doped, and $2|E_F|$ reaches the probe photon energy of 0.86 eV at $V_g = -0.1$ V. Similar curves obtained at different probe photon energies allow us to determine the $2|E_F|$ value of graphene at different applied gate voltages.

Rayleigh scattering intensity from an individual graphene-nanorod hybrid structure as a function of the photon energy and gate voltage is displayed in a two-dimensional (2D) color plot

in Figure 2.4b. and 2.4c shows four line cuts of the 2D plot for Rayleigh scattering spectra at V_g =0.5, -0.1, -0.9, and -1.5V, which clearly demonstrate the capability to modulate surface plasmon resonance through electrical gating. The detailed dependence of plasmon resonance energy (E_R), width (Γ_R), and peak intensity (I_P) on graphene $2|E_F|$ are shown in Figure 2.5a-c (symbols). The resonance width in Figure 2.5b displays a step-like decrease, corresponding to an increase in quality factor, with increasing $2|E_F|$. This is a direct consequence of blocked graphene optical absorption in highly doped graphene, which leads to a reduced $\varepsilon_g^{''}$ in graphene and lower loss. The increased quality factor naturally leads to a higher scattering intensity at the plasmon resonance, as shown in Figure 2.5c. The plasmon resonance frequency exhibits an unusual behavior (Figure 2.5a): it shifts to lower energy, and then to higher energy, with increased graphene doping. This behavior can be accounted for by gated-induced change in the real part of dielectric constant ($\varepsilon_g^{'}$) of graphene, as described in the introduction.

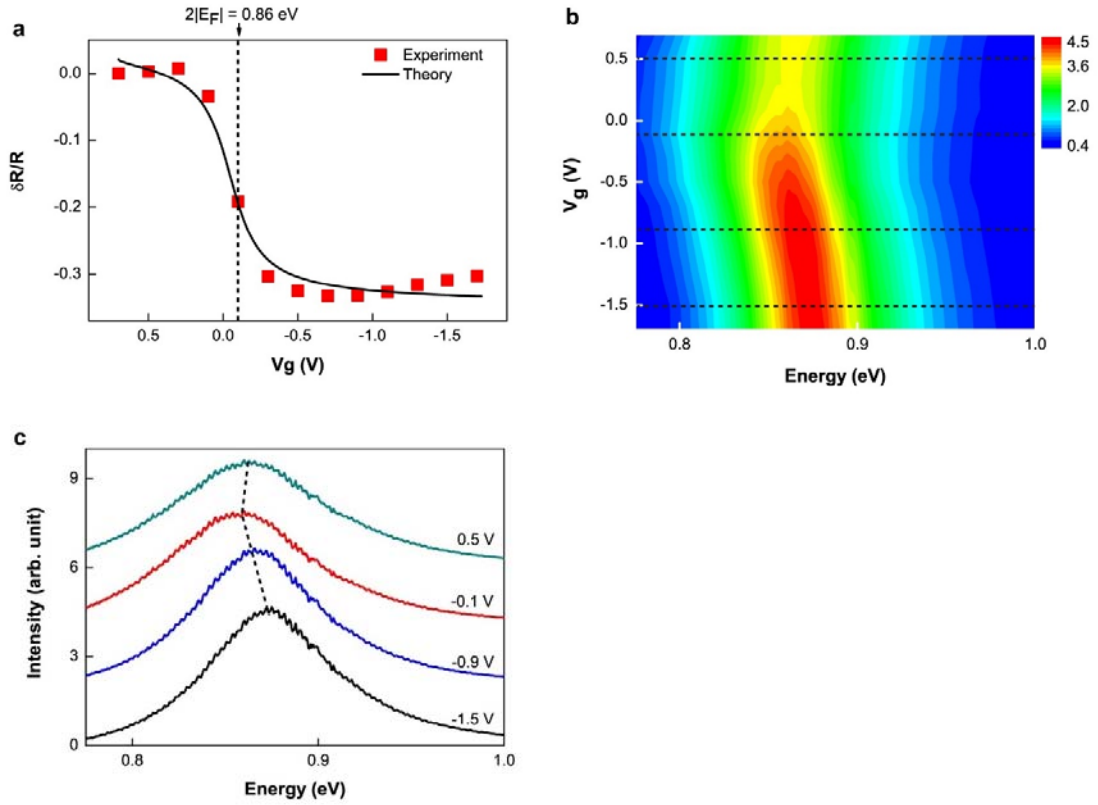

Figure 2.4 Electrical control of the plasmon resonance. a. Gate-induced reflectivity change (δR/R) of graphene on the substrate probed at photon energy of 0.86 eV. It shows a step-function-like decrease in reflectivity, corresponding to a reduction of graphene absorption, due to blocked optical absorption at large hole doping (Fig. 2d). The threshold voltage at $V_g = -0.1$ V is set by $2|E_F|$ reaching the probe photon energy of 0.86 eV. (It indicates that the as-prepared graphene under ionic liquid is strongly hole doped.) **b**. Scattering intensity (color scale, arbitrary units) is plotted as a function of the photon energy and gate voltage. **c**. Rayleigh scattering spectra of an individual graphene-nanorod hybrid structure at V_g=0.5, -0.1, -0.9, and -1.5 V, corresponding to the four horizontal (dashed) line cuts in **b**. Strong modulation of all aspects of the plasmon excitation, including the resonance frequency, quality factor, and scattering intensity, is achieved as electrostatic gating shifts the Fermi energy and modifies optical transitions in graphene.

Figure 2.5a and 5b shows the relation between the changes in the plasmon resonance energy and width with the graphene dielectric constant $\varepsilon_g^{'}$ and $\varepsilon_g^{''}$. I found that the frequency shift

and width increase of the plasmon resonance scale linearly the gate-dependent ε_g' and ε_g'' of graphene, i.e. $E_R = E_R^0 + \alpha\varepsilon_g'$ and $\Gamma_R = \Gamma_R^0 + \beta\varepsilon_g''$ (solid lines in Figure 2.5a and 2.5b). Here $E_R^0 = 862.4\ meV$ and $\Gamma_R^0 = 72.8\ meV$ are the plasmon resonance frequency and width for bare gold nanorod, and $\alpha = -3.693$ and $\beta = 4.828$ are two constant prefactors. (For best fitting I have also slightly shifted $|E_F|$ by 40 meV compared to the values we determined through optical spectroscopy at the region with only graphene. This shift is presumably due to slightly different carrier doping at the hot spot right next to gold.) The simple model reproduces nicely the significant gate-induced decrease of plasmon resonance width (i.e. higher quality factor), as well as the red and blue shifts of the plasmon resonance energy. The increased scattering intensity arises naturally from the increased plasmon resonance quality factor.

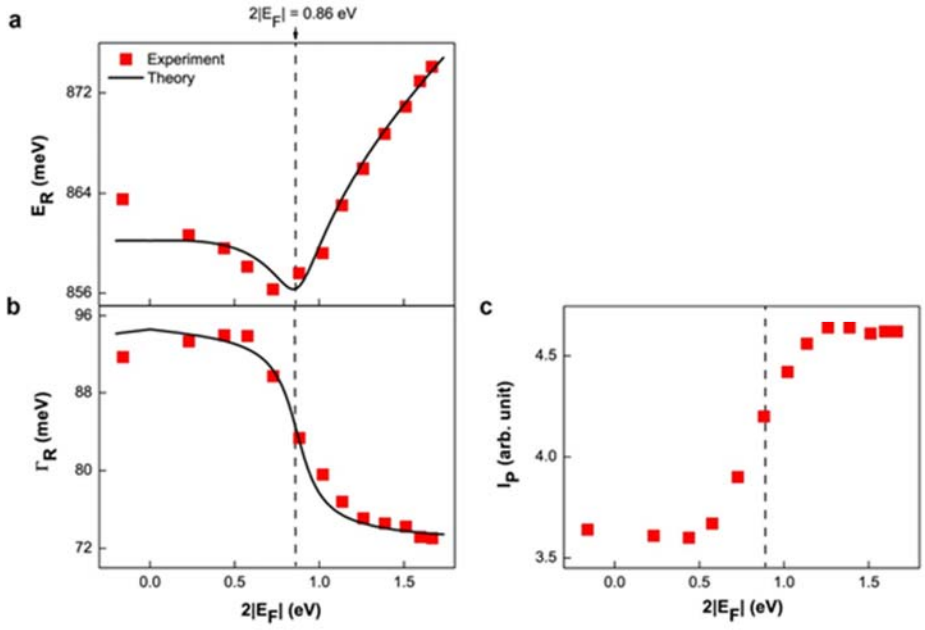

Figure 2.5 Comparison between experiment and theory. Symbols in **a**, **b**, and **c** show, respectively, detailed data of the plasmon resonance energy (E_R), width (Γ_R), and peak scattering intensity (I_P) as a function of $2|E_F|$ in graphene. Our model (solid line) reproduces nicely the experimental data, where the changes in the plasmon resonance

energy and width originate from gate-induced modification in the real ($\varepsilon_g^{'}$) and imaginary ($\varepsilon_g^{''}$) part of graphene dielectric constant, respectively. The red and then blue shift of plasmon resonance frequency in **a** is due to an increase and then decrease of $\varepsilon_g^{'}$ in graphene at the plasmon resonance energy E_R when optical transitions with increasingly higher energies are blocked. This is because interband transitions with energies lower than E_R contributes a negative susceptibility, and transitions with energies higher than E_R contributes a positive susceptibility to $\varepsilon_g^{'}$ at E_R. The decreased resonance width at large $2|E_F|$ in **b** is a consequence of reduced $\varepsilon_g^{''}$ and lower loss when optical transitions at E_R are blocked. This increased quality factor naturally leads to a higher scattering intensity at the plasmon resonance in **c**.

2.3.3 Numerical simulation and possibility as a bio/chemical sensing

The numerical simulation further confirms the above picture. The simulation shows that electrical gating of graphene leads to a modulation of plasmon resonance quality factor by 28% with the gold nanorod placed on top of the graphene layer, which agrees well with our experimental observation. Interestingly, a significant portion of this change arises from the hot spots at the two ends of the gold nanorods due to strongly enhanced electric field therein: Integrated intensity of the in-plane field within the hot spots (defined by two 20nm by 20nm area) constitutes 14% of integrated in-plane intensity overall the whole horizontal plane. It suggests that the small area of graphene at the hot spots 4% increase in plasmon scattering intensity (i.e. 14% of total changes). And this response arise from only ~ 60 gate-induced electrons within the hot spot area given that a carrier concentration variation of $8*10^{12}$ /cm^2 is needed to shift the Fermi energy from 0.4 to 0.5 eV and block interband transition in graphene[4, 15]. Therefore the addition of a single electron at the plasmonic hot spot, such as from charge transfer, can modify nanorod scattering by about $0.7*10^{-3}$. In comparison, the shot-noise limited detection sensitivity is about $10^{-6}/\sqrt{Hz}$ for nanorod plasmon scattering with focused 1mW laser excitation. It suggests that even a single

electron can have a potentially observable effect on gold nanorod plasmon scattering. This extremely strong interaction between graphene and plasmon resonance can enable the detection of individual single charge transfer event at the plasmonic hot spot.

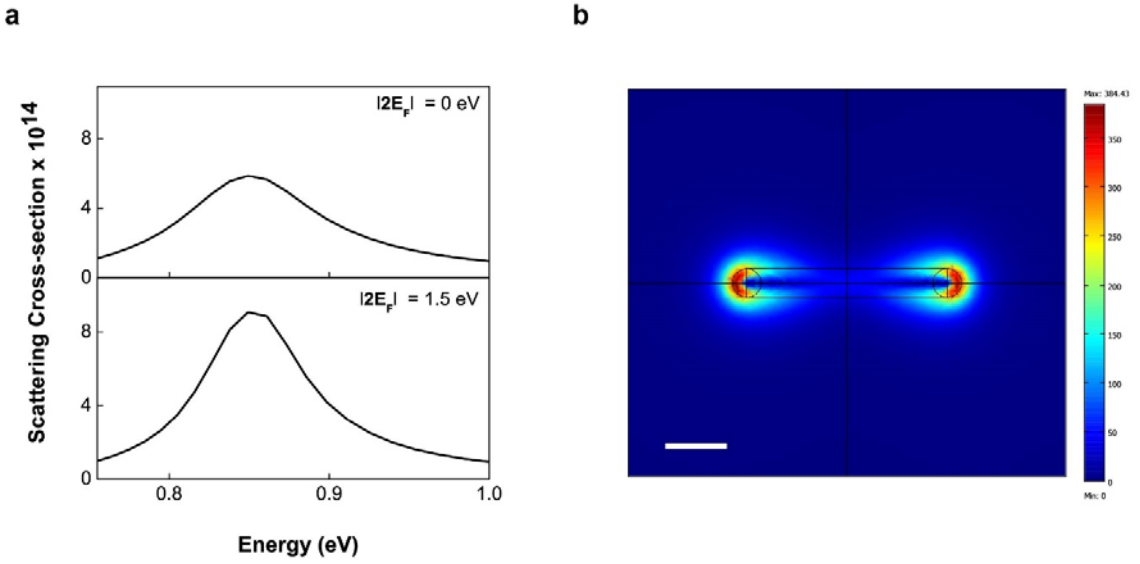

Figure 2.6 Numerical simulation result a. Scattering cross-section change due to the modulation with graphene by gating. Scattering cross-sections are normalized by plane wave incident light. **b.** Distribution of the in-plane scattered electric field magnitude square (V^2 / m^2) on graphene surface where fermi level is at 0.75 eV. White scale bar in the figure corresponds to 50 nm.

2.4 Comparison to hybrid structure with photonic crystal cavity

So far, I have discussed plasmon resonance modulation with gate variable dielectric constant of graphene. Although significant modulation depth is observed in the experiment, it is desirable to further improve the depth. Limitation in modulation depth comes from intrinsic

plasmonic cavity loss in a metal. To be dominated by gate variable graphene absorption, intrinsic cavity loss has to be much smaller than loss due to graphene. Here, I discuss on the effect of graphene on high Q dielectric cavity.

2.4.1 Photonic crystal cavity

The experiments are performed with linear three hole defect (L3) silicon photonic crystal cavities fabricated in Silicon-on-Insulator (SOI) platform. The device thickness d is 250nm, with photonic crystal lattice periodicity a = 450 nm and radius r = 90 nm. The two holes at the end of the cavities are shifted by 0.15a [40]. The photonic crystals are fabricated by electron-beam lithography, followed by plasma etching and finally removing the silicon oxide underneath to make a free standing silicon photonic crystal membrane. On top of the cavities we transferred a large-area graphene grown by chemical vapor deposition using the standard growth and transfer processes[37, 38].

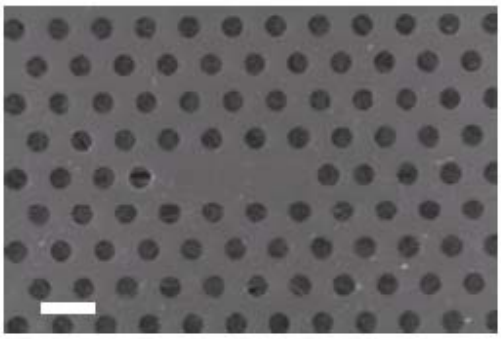

Figure 2.7 Scanning electron micrograph (SEM) of the fabricated cavities with graphene. The scale bars correspond to a 500nm distance.

2.4.2 Effect of graphene on high Q cavity

A quality (Q) factor of ~1000-1500 is observed for the fabricated cavities without graphene. Note that although a much higher quality factor can be obtained in a silicon photonic crystal cavity, I want to keep the quality factor moderate to achieve a relatively large spectral bandwidth. With graphene on top, the Q-factor drastically reduces to ~300-500, as shown in Figure 2.8. The significant broadening of the cavity linewidth arises from graphene absorption. I measure the reflectivity spectrum from several cavities with slightly different r/a ratio. For all the cavities we consistently observe linewidth broadening (Figure 2.8). The quantitative values of the broadening varies slightly in the range of 2 nm to 4 nm, consistent with the theoretical estimation.

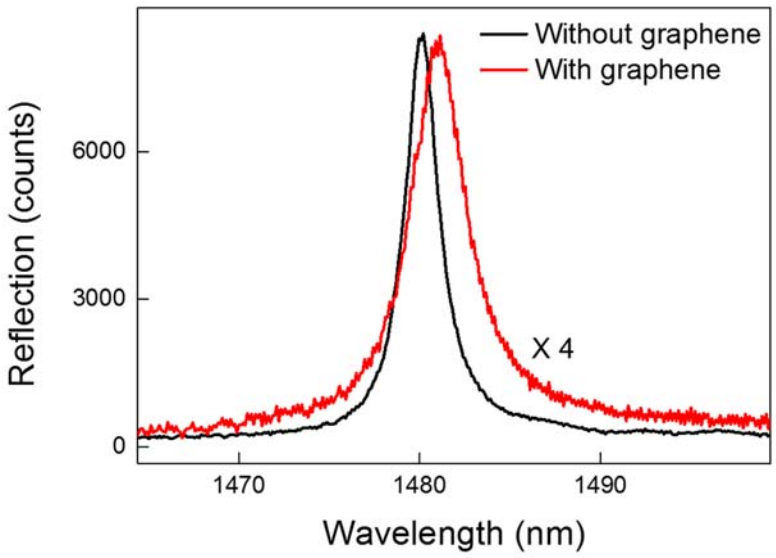

Figure 2.8 Effect of graphene on high Q cavity Significant broadening of the cavity is observed due to graphene absorption.

2.4.3 Possibility as a fast electro-optic modulator

In this section, I theoretically analyze the performance (speed and energy consumption) of such a graphene-photonic crystal cavity modulator with silicon gating. Assuming we need a specific carrier density of n_c (charge/area) to cause significant change in the graphene absorption,

we can write $n_c = CV/q$, where, q is the electronic charge, V is the applied voltage and $C=\varepsilon/d$ is the capacitance per unit area, and d is the alumina thickness. The total capacitance will be $C_T = CA$, with A being the gated graphene area. Hence the total energy E_T consumption for the modulator will be $1/2\ C_T\ V^2$. This means

$$E_T = \frac{1}{2}CAV^2 = \frac{Aq^2{n_c}^2 d}{2\epsilon}$$

In a graphene-PhC modulator we can achieve: A = 1 μm^2 (assuming that the lithographically defined graphene covers only the cavity region), alumina thickness d=5 nm, dielectric constant of Alumina is 10, and the carrier density in graphene required to do such modulation is 10^{17} /m^2, then the capacitance of the device becomes C_T = 17fF. Such a low capacitance is the key for low energy and high speed operations. For high frequency operations, the parasitic capacitance of the metal wire on the alumina on silicon will limit the performance. To circumvent that, one needs to dope the silicon selectively, and reduce the overlap between graphene and doped silicon only to the cavity region.

With a device capacitance of 17fF the energy of the modulator is around 8 fJ. The speed of the device will be limited by the RC constant of the device. The resistance of the device will come mostly from the graphene resistance, assuming the silicon is highly doped, and is of very low resistance. Again, one needs to bring the electrodes closer to the cavity to reduce the resistance. Such nano-fabrication is already demonstrated in GaAs photonic crystal cavity[41] and can be easily extended to the SOI platform. In our device, the graphene resistance is around 500Ω (including the contact resistance), leading to a device speed of ~20GHz. However, the dc conductivity of graphene in strongly doped region, as used in the modulator condition[27], can be quite high. Sukang Bae et. al. has shown a sheet resistivity of 30Ω/sq[42]. Assuming the length

and width of the graphene electrode are ~1 micron, we find that the resistance of the device can be as low as 30Ω and the speed of the modulator can be over 100 GHz.

2.5 Conclusion

In summary, I experimentally demonstrate electro-static tuning of graphene clad nanophotonic resonators. With an increased light-matter interaction in cavity, even a single atom thick graphene can significantly modify the nanophotonic resonators. I believe such tunability can be exploited in conjunction with other nano-photonic structures for various applications such as bio/chemical sensing, optical interconnect, phased array optical antenna, or 3-D display.

Chapter. 3 Ultrafast generation of pseudomagnetic field for valley excitons in WSe2 monolayers

3.1 Introduction

Atomically thin layers of transition metal dichalcogenides (MX_2) have emerged as an exciting two-dimensional semiconductor platform for nanoelectronics and optoelectronics[43, 44]. In particular, a pair of degenerate bands are present at the K and K' valleys in the momentum space of hexagonal MX_2 monolayers, giving rise to a unique valley degree of freedom that is analogous to electron spin[8]. Recent polarization-resolved photoluminescence (PL) studies show that the valley pseudospin in MX_2 can couple directly to the helicity of excitation photons[45-48], and the pseudospin polarization between two valleys exhibits a remarkable coherent behavior[48]. It raises the intriguing prospect of valleytronics that exploits the valley degree of freedom to carry information[43, 49, 50].

Just as spin manipulation in spintronics, the capability to control the valley pseudospin is essential for valleytronics based on MX_2 materials. In spintronics, the electron spin can be manipulated through any external perturbation that breaks the energy degeneracy of two orthogonal spin polarizations. This can be achieved either through an external magnetic field, the most common approach[51, 52], or through a pseudo-magnetic field generated by other stimuli. For example, circularly polarized light can produce a pseudo-magnetic field and rotate the electron spin through the optical Stark effect. (The optical Stark effect, a well-established phenomenon in

atomic physics and quantum optics, describes the energy shift in a two-level system induced by a non-resonant laser field.) Such pseudo-magnetic field generated by spin-selective optical Stark effects has been demonstrated as an effective and ultrafast way to manipulate electron spins in semiconductor quantum wells and quantum dots[53, 54]. It will be highly desirable to realize similar control of valley excitons in MX_2 using light-induced pseudo-magnetic field for valleytronics.

In this chapter, I demonstrate a valley-selective optical Stark effect in monolayer WSe_2 to generate ultrafast and ultrahigh pseudo-magnetic field for valley excitons. Previously, resonant pump-probe spectroscopy has been used to probe ultrafast carrier dynamics after the pump photons are absorbed by exciton transitions in MX_2 monolayers[55-57]. Here I employ non-resonant circularly polarized laser pumping with photon energies below the bandgap, which induces a coherent and dissipationless valley-selective optical Stark effect for pseudospin manipulation. I show that transition energies of the degenerate exciton resonances at K and K' valleys can be selectively shifted using circularly polarized laser pulses. The optical Stark energy shift happens instantaneously at the presence of a pump pulse, and its magnitude shows systematic dependence on the pump intensity and detuning. The light-induced valley exciton energy splitting can be as large as 10 meV, which corresponds to a pseudo-magnetic field ~60 Tesla. Such valley-selective optical Stark shift will be enabling for ultrafast and all-optical control of the valley polarization in atomically thin MX_2 layers.

3.1.1 Optical Stark effect

Optical Stark effect is well-understood phenomenon in the context of atomic physics and quantum optics. Manipulation of cold atoms and trapped ions and coherent control of

superconducting qubits and electron spins are achieved via optical Stark effect. In a two-level system, the optical Stark effect can be readily understood using the dressed atom picture. Consider the two-level system composed of the ground state and excited state. Figure 3.1 illustrates the effect of light whose energy is below the resonance. In the dressed atom picture, the dressed ground state (with N σ_+ photons) and the two-level system are coupled by the dipole interaction, which leads t wavefunction hybridization and energy level repulsion. It effectively shifts down the ground state energy and shifts up the excited state energy.

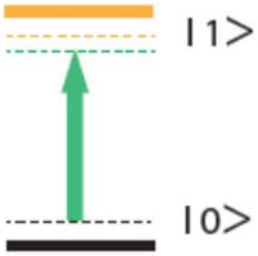

Figure 3.1 Illustration of optical Stark effect Yellow and black dashed line represent unperturbed two level system. In the presence of pump photon (green arrow), energy levels repel each other (solid lines).

3.1.2 Valley-selective dipole interaction in MX2

Valley states in MX2 are degenerate since they are time-reversal pairs. However, they have distinctive optical selection rules and couple to photons of opposite helicity. The dipole transition matrix element of the K-valley A-exciton is characterized by $P_K^{\sigma\pm} = \langle K|\hat{p}_x \pm i\hat{p}_y|0\rangle$, where $|K\rangle$ and $|0\rangle$ correspond to the K-valley A-exciton and ground state, respectively, $\hat{p}_x, \hat{p}_y$ are momentum operators, and σ_+ / σ_- corresponds to left/right circular light. In MX_2 monolayers $P_K^{\sigma+}$ has a finite value but $P_K^{\sigma-}$ is approximately zero. Consequently, the A-exciton at the K valley couples exclusively to left-circularly polarized light. The A-exciton at the K' valley, on the other hand, couples only to the right-circularly polarized light. This dipole selection rule for valley

transitions in monolayer WSe_2 governs both resonant and non-resonant excitations, which can have different manifestations in valley physics. I will discuss more detailed later with experimental data.

3.2 Experiment

3.2.1 Photoluminescence and linear absorption measurement

For photoluminescence (PL) measurement, I used a 690 nm laser (photon energy = 1.8 eV) to excite a WSe_2 monolayer. The laser beam was focused to a diffraction-limited spot with a diameter ~ 1 μm, and the PL was collected in the reflection geometry using a confocal microscope. A monochromator and a liquid-nitrogen cooled CCD were used to record the PL spectra.

For linear absorption measurement, a supercontinuum laser (Fianium SC450) was used as broadband light source. The laser was focused at the sample with ~2 μm beam size and the reflection signal R was collected and analyzed by a spectrometer equipped with a one-dimensional CCD array. The reference spectrum R_0 was taken on the sapphire substrate nearby the WSe_2 monolayer sample. The normalized difference signal $(R-R_0)/R_0$ is directly proportional to the linear absorption from atomically thin layers on sapphire.

3.2.2 Transient absorption spectrum measurement (Pump-probe spectroscopy)

To observe valley-selective optical Stark effect, I perform polarization-resolved femtosecond pump-probe spectroscopy. With the control of time delay between pump and probe pulse of different energy, one can obtain transient absorption spectra. Furthermore, employing

circular polarization control for pulses allows to monitor optical transition at K and K' point selectively.

Femtosecond pulses for pump and probe are prepared as following. Femtosecond pulses at 1026 nm were generated by a regenerative amplifier seeded by a mode-locked oscillator (Light Conversion PHAROS). The femtosecond pulses (at a repetition rate of 150 kHz and a pulse duration ~250 fs) were split into two parts. One part was used to pump an optical parametric amplifier (OPA) to generate tunable excitation laser pulses, and the other part was focused into a sapphire crystal to generate a supercontinuum white light (500 nm ~ 900 nm) for probe pulses.

For atomically thin materials on a transparent sapphire substrate, the reflection change $\Delta R/R$ is directly proportional to the change in absorption coefficient[58]. In order to observe valley-selective optical Stark effect, a femtosecond pulse (pump) first induces energy shift in a monolayer WSe2, and the photo-induced changes in the reflection spectrum ($\Delta R/R$), i.e. absorption spectrum, are probed by a laser-generated supercontinuum light after controlled time delays.

The pump and probe beams were focused at the sample with a diameter of 16 μm and 8 μm, respectively. The probe light was detected by a high-sensitivity photomultiplier after wavelength selection through a monochrometer with spectral resolution of 1 nm. The pump-probe time delay was controlled by a motorized delay stage, and the pump-probe signal was recorded using the lock-in detection with a chopping frequency of 1.6 kHz. The polarization of pump and probe pulses was independently controlled using broadband quarter-wave plates and linear polarizers.

3.2.3 CVD-grown monolayer WSe2 sample

For experiment, I used triangular monolayers of WSe2 grown by chemical vapor deposition (CVD) on sapphire substrates (Figure 3.2). WO3 and selenium powders are sublimed in a horizontal tube furnace. The WO3 was placed at the center of the tube furnace and heated to 925^{o}C and the selenium was placed at the upstream side of the tube furnace and maintained at 290^{o}C *via* a heat tape. Selenium vapor was transported to the hot zone with the gas mixture 60 sccm of Ar and 6 sccm of H_2, while the pressure was maintained at 7 Torr during the growth. The triangular WSe_2 flakes were grown on the sapphire substrates located at the downstream side from WO_3.

Figure 3.2 Optical micrograph of a monolayer WSe2 on sapphire substrate Scale bar corresponds to 25 um.

3.3 Result and discussion

3.3.1 Optical transition in a monolayer WSe2

The optical reflection spectrum of monolayer WSe_2 at 77 K exhibits two prominent resonances at 1.68 eV and 2.1 eV (Figure 3.3), which correspond, respectively, to the A- and B-

excitons split by the spin-orbital coupling[43]. In this study, I focused on the lowest energy A-exciton transition. This A-exciton is well separated from other excited states in energy due to strong electron-hole interactions in monolayer WSe_2. As a result, the ground state and the A-exciton can be approximated as a two-level system and neglect the effect from other excited states.

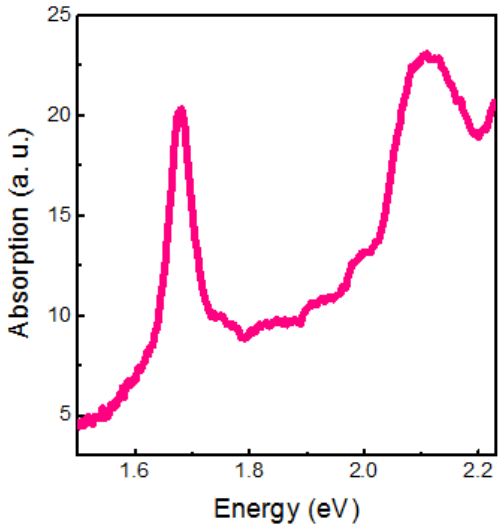

Figure 3.3 Absorption spectra of a monolayer WSe2 The optical reflection spectrum of a WSe_2 monolayer on a sapphire substrate at 77 K, which exhibit strong A- and B-exciton resonances at 1.68 eV and 2.1 eV, respectively.

3.3.2 Circular polarization dependent photoluminescence

The valley-dependent resonant excitation enables both the generation of a valley-polarized exciton population through the absorption of circularly polarized light and the detection of valley-polarized excitons through polarization-resolved photoluminescence (PL)[43]. Figure 3.4 displays polarization-resolved PL spectra of our WSe_2 samples upon laser excitation at 1.8 eV with σ_+ circular polarization, where the PL intensity with helicity matching the excitation light (σ_+, red curve, Figure 3.4A) is about four times stronger than that for the opposite helicity (σ_-, blue curve,

Figure 3.4B). This behavior is similar to that reported in previous studies[43], and verifies the valley-selective excitation and emission in our WSe_2 monolayers. The non-zero σ_- polarized PL is presumably due to a finite intervalley scattering because the excitation energy is ~120 meV higher than the A-exciton resonance.

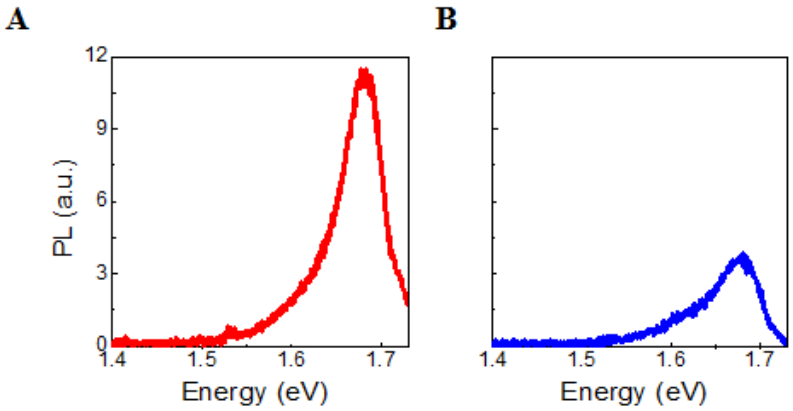

Figure 3.4 Circular polarization dependent photoluminescence spectra Polarization-resolved PL spectra of a WSe_2 monolayer at 77K. For 1.8 eV excitation laser with left circular polarization, the PL spectra show a prominent emission peak at the A-exciton resonance (1.68 eV), and the PL intensity with left circular polarization (red curve, A) is about four times stronger than that with right circular polarization (blue curve, B). It demonstrates that valley-polarized A-exciton population can be created by circularly polarized resonant excitation, and it can be detected by polarization-resolved PL spectroscopy.

3.3.3 Valley-selective optical Stark effect

I measured the valley-selective optical Stark shift in WSe_2 monolayers with non-resonant circularly polarized excitation using pump-probe spectroscopy as explained previously. Femtosecond pump pulses with tunable photon energies below the A-exciton resonance were generated by an optical parametric amplifier. Optical Stark shifts of the WSe_2 exciton transitions induced by the pump pulses was then probed in transient reflection spectra over the spectral range

of 1.59-1.77 eV using a laser-generated supercontinuum light. Figure 3.5B and 3.5C display two-dimensional plots of transient reflection spectra in a monolayer WSe_2 with σ_+ and σ_- polarized probe light, respectively, upon σ_+ polarized pump excitation. Here the non-resonant pump photons are at 1.53 eV, which is 150 meV below the exciton resonance and do not excite any real transitions. The color scale in Figure 3.5B and 3.5C represents the relative reflectivity change $\Delta R/R$, the horizontal axis shows the probe photon energy, and the vertical axis shows the pump-probe time delay. For atomically thin WSe_2 layers on a transparent sapphire substrate, the reflection change $\Delta R/R$ is directly proportional to the change in the absorption coefficient[58]. It is apparent that strong changes in the exciton absorption are present only for σ_+ probe pulses (Figure 3B), and no pump-induced signals can be detected above the noise level for σ_- probe pulses (Figure 3C). This indicates that the non-resonant σ_+ pump significantly modifies the A-exciton transition at the K valley, but not at the K' valley.

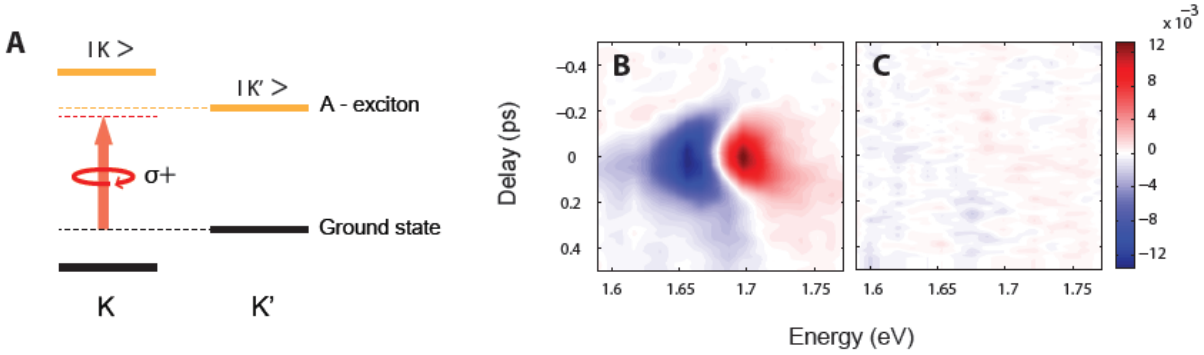

Figure 3.5 Valley-dependent optical Stark effect with non-resonant circularly polarized pump. (A) Schematic illustration of the optical Stark effect for valley transitions with non-resonant, left circularly polarized σ_+ pump. The dashed black and yellow lines denote the unperturbed ground and exciton states, respectively, and the pump photon energy is lower than the exciton resonance energy (red arrow). In the dressed atom picture, the dressed ground state (with N σ_+ photons) and the K-valley A-exciton (with N-1 σ_+ photons) are coupled by dipole transition, which results in energy level repulsion (solid black and yellow lines on the left section) and an increased exciton transition energy.

On the other hand, σ_+ pump does not affect K'-valley A-exciton resonance due to optical selection rule (right section). **(B) and (C)** Transient reflection spectra of A-exciton resonance at 77 K. The color scale, horizontal axis, and vertical axis represent the relative reflectivity change ΔR/R, the probe photon energy, and the pump-probe time delay, respectively. For atomically thin WSe_2 on sapphire substrate, ΔR/R is proportional to absorption change. Non-resonant σ_+ pump of photon energy at 1.53 eV leads to a strong transient absorption signal for probes with the same polarization σ_+ **(B),** but produces no transient response for probes with the opposite polarization σ_- **(C)**. It demonstrates that non-resonant σ_+ pump significantly modifies A-exciton transition at the K valley, but not at the K' valley.

To better examine the time evolution and spectral lineshape of the photo-induced transient reflection spectra in WSe_2 monolayers, we plot in Figure 3.6 vertical and horizontal linecuts of the two-dimensional plot for the σ_+ pump and σ_+ probe configuration (Figure 3.5B). Figure 3.6A displays the transient reflection signals at the probe photon energy below (1.65 eV, blue line) and above (1.7 eV, red line) the exciton resonance at different pump-probe delay τ (vertical linecuts in Figure 3.5B). Both signals have the largest magnitude at τ=0 and show a symmetric rise and decay dynamics. This is characteristic of an instantaneous response with the rise/decay time limited by the laser pulse width of ~ 250 fs. It shows that the exciton absorption is modulated only when the pump radiation is present. In addition, the transient reflectivity has opposite signs for probe energies at 1.65eV and 1.7 eV. Detailed transient reflection spectrum ΔR/R, which is proportional to the transient absorption change, is shown in Figure 3.6B (green circles) for τ=0 through a horizontal linecut in Figure 3.5B. We observe that the transient absorption signal changes sign at exactly at the A-exciton resonance energy E_A=1.68 eV. The pump laser leads to reduced absorption below E_A and increased absorption above E_A, which matches well the linear derivative of the WSe_2 monolayer absorption spectrum (magenta line in Figure 3.6B). Quantitatively, the photo-induced absorption change can be perfectly described by a simple blueshift of ~ 4 meV of the K-valley

exciton resonance. The magnitude of exciton energy shift (ΔE) can be estimated directly through $\Delta E = (\frac{d\alpha}{dE})^{-1}\Delta\alpha$.

The blueshift in transition energy, instantaneous time response, and valley selectivity demonstrate unambiguously the optical Stark effect in monolayer WSe_2 upon non-resonant pump excitation. We note that the photo-induced signal becomes non-detectable immediately after the pump pulses, indicating negligible dissipative processes associated with real exciton absorption. We also performed the pump-probe spectroscopy using linearly polarized pump and probe pulses. Here photo-induced absorption changes are of similar magnitude independent of the pump and probe polarizations. This is because the linear-polarized pump has both σ_+ and σ_- components, which lead to optical Stark shifts for both K and K' valley exciton transitions.

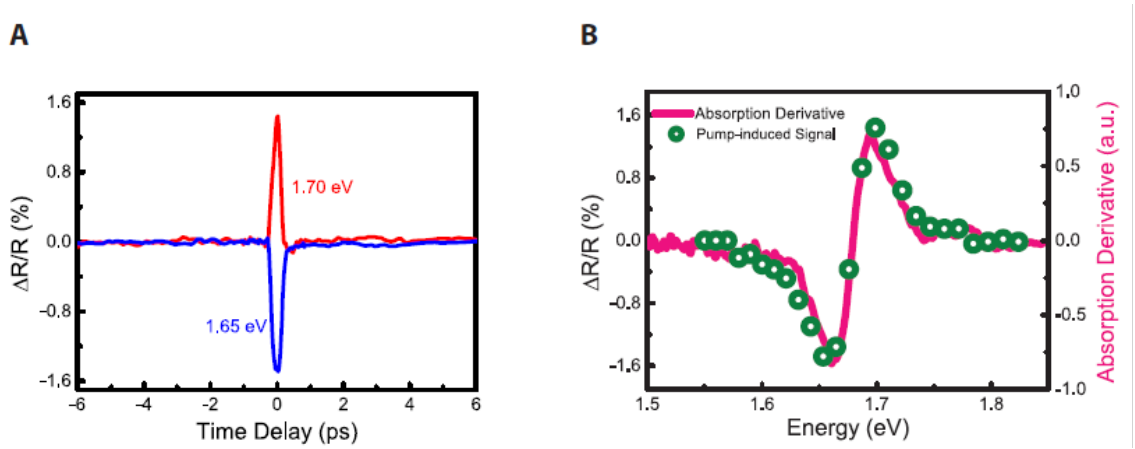

Figure 3.6 Time evolution and spectral lineshape of the valley-dependent transient reflection spectra for σ_+ pump and σ_+ probe configuration. **(A)** Time evolution of the pump-induced transient reflectivity ΔR/R at probe energies of 1.65 eV (blue line) and 1.7 eV (red line). Both signals reach the maximum magnitude at the pump-probe delay τ=0 with symmetric rise and decay dynamics (limited by our pulse width ~250 fs), which is characteristic of an instantaneous optical response. The transient reflectivity has opposite signs for 1.65 eV and 1.7 eV probes. **(B)** The transient reflection spectrum at τ=0 (green circles). The transient reflectivity signal changes sign at the A-exciton resonance energy E_A=1.68 eV, and it shows a dispersive line shape. This transient reflection spectrum matches well

with the derivative of linear absorption spectrum in monolayer WSe_2, and can be fully accounted for by a 4 meV blueshift of the K-valley A-exciton resonance (magenta line).

3.3.4 Control of energy shift with pump power and detuning

Next I examine how the valley-selective optical Stark shift varies with the pump laser intensity and detuning. The pump detuning $\hbar\Omega$ is defined as the difference between the exciton resonance energy ($\hbar\omega_0$) and the pump photon energy ($\hbar\omega_p$). Figure 3.7 shows the transient reflection data (left axis) and the corresponding energy shift of the A-exciton energy (right axis) at the K valley for σ_+ pump and σ_+ probe configuration with different pump detuning (green dots in Figure 3.7A) and pump intensities (green dots in Figure 3.7B). We observe that the optical Stark shift is inversely proportional to the pump detuning (magenta dashed line in Figure 3.7A), and scales linearly with the laser intensity (magenta dashed line in Figure 3.7B). Such scaling matches well with the theoretical prediction of optical Stark shift $\delta(\hbar\omega_0) = 2S \cdot E_p^2/\hbar\Omega$, where S is the optical Stark shift constant related to the transition dipole moment and E_p is the electric field of the pump pulse[59]. From the experimental data, we can determine an optical Stark shift constant S ~ 45 $Debye^2$ for A-exciton in monolayer WSe_2, which is of similar magnitude to that for exciton transition in semiconductor quantum wells[60, 61].

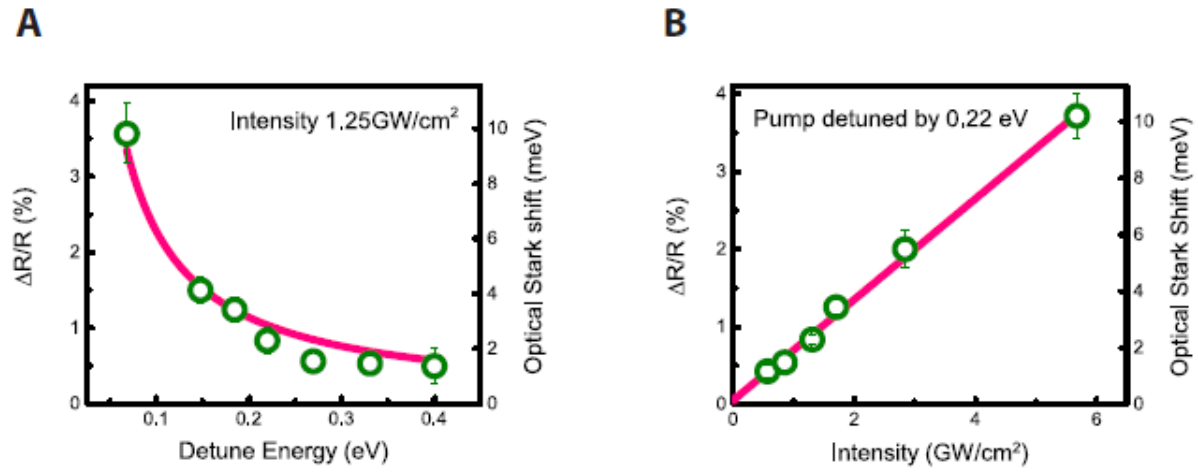

Figure 3.7 Pump detuning and pump intensity dependence of the valley-selective optical Stark shift. (A) The transient reflection signal at 1.7 eV (left axis) and the corresponding optical Stark shift (right axis) as a function of the pump detuning energy (green dots). The dependence can be nicely described by an inverse proportional relationship (magenta line). **(B)** The transient reflection signal at 1.7 eV (left axis) and the corresponding optical Stark shift (right axis) as a function of the pump laser intensity (green dots), which shows a linear scaling behavior (magenta line). The optical Stark shift can selectively shift the K-valley exciton transition by as much as 10 meV, which corresponds to a valley pseudo-magnetic field of ~ 60 T.

3.3.5 Estimation of pseudomagnetic field magnitude

The valley-selective optical Stark shift breaks the degeneracy of valley exciton transitions in monolayer WSe_2 and defines an effective valley pseudo-magnetic field. In the experiment, the photo-induced energy splitting between K and K' exciton transitions can be as large as 10 meV (Figure 3.7). The corresponding pseudo-magnetic field B_{eff} for valley excitons can be estimated by $B_{eff} = \frac{\Delta E}{2 g_{ex} \mu_B}$, where μ_B is the Bohr magneton and g_{ex} is the effective g-factor for valley exciton transitions in WSe_2. The effective exciton g-factor g_{ex} combines contributions from both electrons and holes, and has a theoretically predicted value ~ 1.5 for WSe_2[62, 63]. Using this g-factor, we estimate a pseudo-magnetic field B_{eff} as high as 60 T for a 10 meV splitting of valley exciton transitions. A real magnetic field of this magnitude is difficult to achieve even with

superconducting magnets, but such a pseudo-magnetic field for MX_2 valley excitons can be produced conveniently and with femtosecond temporal control using light pulses.

3.4 Conclusion and outlook

In summary, I demonstrate that the optical Stark effect can generate ultrafast and ultrahigh pseudo-magnetic field for valley excitons in MX_2 layers. It has been reported recently that excitons in different valleys in monolayer WSe_2, resonantly excited by linear polarization light, can maintain their phase coherence over extended time[48]. The valley-dependent optical Stark effect offers a convenient and ultrafast way to lift the valley degeneracy and introduce a controlled phase difference between the two valley states, therefore enabling coherent rotation of resonantly excited valley polarizations with high fidelity. In analogy with spintronics, such coherent manipulation of valley polarization can open up fascinating opportunities for valleytronics.

Chapter. 4 Ultrafast charge transfer in MoS2/WS2 heterostructure

4.1 Introduction

Atomically thin 2D crystals constitute a rich family of materials ranging from insulators and semiconductors to semi-metals and superconductors[2]. Heterostructures from these 2D materials offer a new platform for exploring new physics like superlattice Dirac points and Hofstadter butterfly pattern[64-66], and new devices like tunnelling transistors[67], memory devices[68] and ultrathin photodetectors[69]. Van der Waals heterostructures of semiconducting MX_2 layers are particularly exciting for optoelectronic and light harvesting applications because many MX_2 monolayers are direct-bandgap semiconductors[6, 7] with remarkably strong light-matter interactions[69, 70]. And importantly, MX_2 heterostructures are predicted to form type-II heterojunctions that can assist efficient separation of photoexcited electrons and holes[71-74].

In type-II heterojunctions, the conduction band minimum and valence band maximum reside in two separate materials. Photoexcited electrons and holes therefore prefer to stay at separate locations. Figure 4.1 illustrates the alignment of electronic bands of MoS_2 and WS_2 monolayers predicted by a recent theory[73]. It shows that monolayer MoS_2 and WS_2 has a bandgap of 2.39 eV and 2.31eV, respectively, and the MoS_2 valence band maximum is 350 meV lower than that of WS_2. Consequently, the MoS_2/WS_2 heterostructure forms a type-II heterojunction (if we neglect the hybridization of electronic states in MoS_2 and WS_2 layers), with

the conduction band minimum residing in MoS_2 and the valence band maximum in WS_2, respectively. In the single-particle picture, this heterojunction will lead to efficient charge transfer with separated electrons and holes in two layers upon optical excitation (Figure 4.1), which can have a dominating effect on both light emission and photovoltaic responses in MoS_2/WS_2 heterostructures.

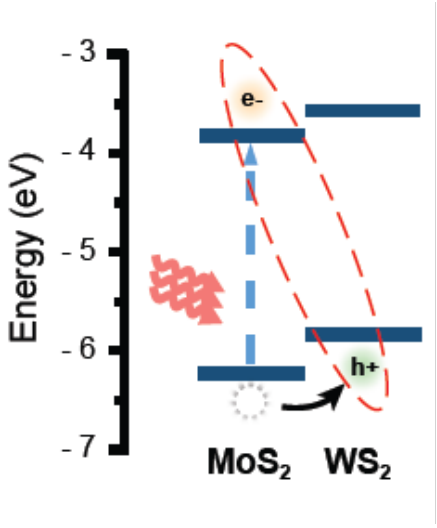

Figure 4.1 Band alignment and structure of MoS_2/WS_2 heterostructures. a. Schematics of theoretically predicted band alignment of a MoS_2/WS_2 heterostructure, which forms a type-II heterojunction. Optical excitation of the MoS_2 A-exciton will lead to layer separated electron and hole carriers.

There are two outstanding questions regarding charge transfer processes in the atomically thin and van der Waals-coupled MoS_2/WS_2 heterostructure. (1) How do strong electron-electron interactions and excitonic effects affect charge transfer processes? (2) How fast can charge transfer take place between van der Waals-coupled layers? Electron-electron interactions are dramatically enhanced in 2D materials due both to size confinement and inefficient screening. Theoretical studies[75, 76] have predicted an exciton binding energy from 500 meV to 1 eV in MX_2 monolayers, which is larger than the expected band displacement of 350 meV in MoS_2/WS_2

heterostructure. Therefore the exciton cannot dissociate into a free electron and a free hole in two separate layers. Will this large exciton binding energy then prevent charge transfer processes and keep the exciton in one layer, or will a new bound state of layer-separated electron and hole pair be generated? In addition, van der Waals coupling is rather weak compared to covalent bonding. Will that lead to a much slower charge transfer process in van der Waals heterostructures compared to their covalent counterparts? Previous studies in organic photovoltaics (OPV)[77-79] have shown that ultrafast charge transfer and separation can take place in organic/organic van der Waals coupled interfaces. However, the 2D MX_2 heterostructures possess two-dimensional crystalline structures and atomically sharp interfaces, which is fundamentally different from the OPV molecular systems. So far little is known about the ultrafast charge transfer dynamics in these new 2D heterostructures.

In this chapter, I study charge transfer dynamics in MoS_2/WS_2 heterolayers experimentally. Through combined photoluminescence spectroscopy and optical pump-probe spectroscopy, we demonstrate that ultrafast charge transfer takes place very efficiently in MoS_2/WS_2 heterostructures. In particular, holes in the MoS_2 layer can separate into the WS_2 layer within 50 fs upon photo-excitation.

4.2 Experiment

4.2.1 Photoluminescence and Raman spectrum measurement

For photoluminescence mapping, I use a 532 nm laser (photon energy =2.33 eV) to excite the isolated monolayers of MoS_2, WS_2, and MoS_2/WS_2 heterostructures. The laser beam is focused

to a diffraction-limited spot with a diameter ~ 1 μm, and the PL is collected in the reflection geometry via confocal microscope. A monochrometer and a liquid nitrogen cooled CCD are used to record the PL spectra. Two-dimensional PL mapping is done by scanning the computer-controlled piezoelectric stage. For Raman measurements, we use a 488 nm excitation laser.

4.2.2 (Transient) Absorption spectrum measurement

I use the same experimental configuration as described in chapter 3.

4.2.3 Heterostructure preparation

The heterostructure was prepared by transferring[80] monolayer MoS_2 onto monolayer WS_2 on sapphire. The CVD grown MoS_2 single layer (described above) on SiO2/Si is spin-coated with PMMA (A4) at 4000 rpm for 60 seconds. PMMA/ MoS_2 film is separated from the substrate (SiO2/Si) by KOH etching (1 mol/L) at 80 ˚C. The film is transferred to DI water beakers to dilute KOH residue under MoS_2. Then, it is transferred on to CVD grown WS_2 on sapphire substrate (described above) and soaked in acetone to dissolve PMMA. Finally, heterostructure sample is annealed at elevated temperature in vacuum. Note there is no polymer between the MoS_2 and WS_2 layers in our sample after the PMMA transfer (PMMA was on top of the top layer), and they can form fairly good contract.

4.3 Result and discussion

4.3.1 Optical micrograph of sample and Raman spectra

Figure 4.2a schematically shows our sample configuration. In brief, MoS_2 monolayers

were grown on 285 nm SiO_2/Si substrates using the chemical vapour deposition (CVD) method[80]. They were subsequently transferred on top of as-grown CVD WS_2 flakes on sapphire substrates[81] to form MoS_2/WS_2 heterostructures. Raman spectra (Figure 4.2b) from isolated MoS_2 and WS_2 films confirm that both are monolayers because the energy separation between Raman active modes agrees well with previous reported values for monolayer MoS_2 and WS_2.[82-85] The Raman spectrum of a MoS_2/WS_2 heterostructure (Figure 4.2b) appears to be an addition of Raman modes from the constituent layers.

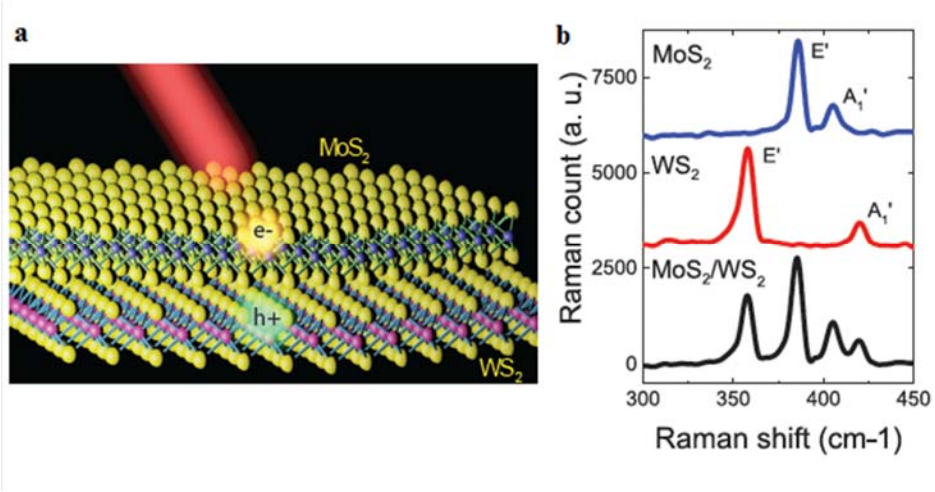

Figure 4.2 Schematic of heterostructure and Raman spectra a. Illustration of a MoS_2/WS_2 heterostructure with a MoS_2 monolayer lying on top of a WS_2 monolayer. Electrons and holes created by light are shown to separate into different layers. **b.** Raman spectra of an isolated MoS_2 monolayer (blue trace), an isolated WS_2 monolayer (red trace), and a MoS_2/WS_2 heterostructure (black trace).

4.3.2 Photoluminescence spectrum and mapping of heterostructure

One sensitive probe of charge transfer in MX_2 heterostructures is photoluminescence (PL) spectroscopy, because an electron and hole pair spatially separated in two MX_2 layers cannot emit efficiently. We performed PL spectroscopy and mapping on multiple MoS_2/WS_2 heterostructure

samples. Figure 4.3a displays the optical image of one sample where a large continuous MoS_2 piece (covering everywhere in the image) was transferred on top of WS_2 flakes (the bright areas). Figure 4.3b shows the PL intensity map at the MoS_2 A-exciton resonance (1.93 eV) at 77 K when the sample is excited by 2.33 eV photons. We observed strong PL signals in the MoS_2-only region, but the PL is significantly quenched in the MoS_2/WS_2 heterostructure region. Figure 4.3c further displays typical PL spectra for MoS_2/WS_2 heterostructures, isolated MoS_2, and isolated WS_2 layers with 2.33 eV excitation. It is apparent that MoS_2 and WS_2 monolayers show strong PL at their respective A-exciton resonances (1.93 eV and 2.06 eV), but both PL signals are efficiently quenched in MoS_2/WS_2 heterostructures. Room temperature PL spectra also exhibit similar behaviour. In principle, PL signals can be quenched by two mechanisms in a heterostructure: energy transfer and charge transfer. However, energy transfer quenches only the PL from a higher energy transition (i.e. 2.06 eV resonance in WS_2), but tends to enhance luminescence from the lower energy transition (i.e. 1.93 eV resonance in MoS_2). On the other hand, charge transfer will quench light emission from all transitions. Therefore the observation of reduced PL from both WS_2 and MoS_2 exciton resonances in MoS_2/WS_2 heterostructures demonstrates that efficient charge transfer takes place in this type-II heterojunction.

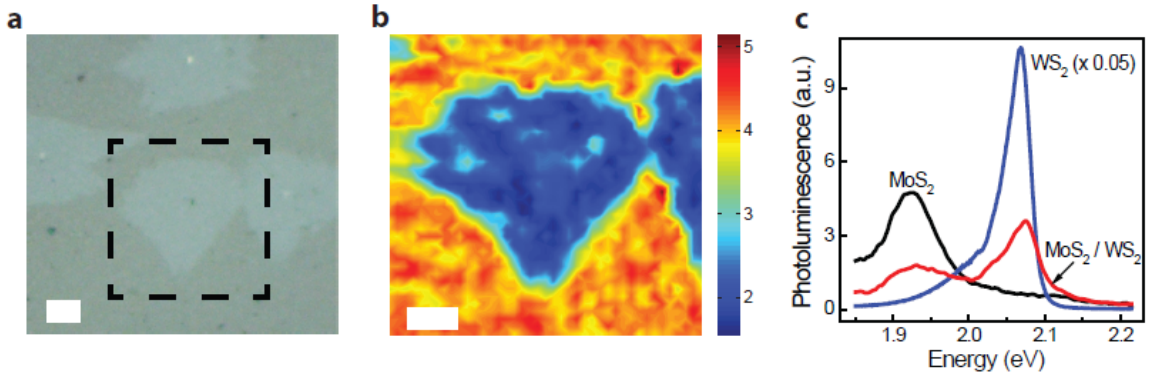

Figure 4.3 Photoluminescence (PL) spectra and mapping of MoS_2/WS_2 heterostructures at 77 K. a. Optical microscope image of a typical MoS_2/WS_2 heterostructure sample. The MoS_2 layer covers everywhere in the image, and bright areas correspond to MoS_2/WS_2 heterostructures. **b.** PL mapping data taken in the dashed rectangle area in **a**. The colour scale represents PL intensity at the MoS_2 A-exciton resonance (1.93 eV). It clearly shows that MoS_2 PL is strongly quenched in the heterostructure. Scale bar is 5 μm. **c.** Typical PL spectra of an isolated monolayer MoS_2, an isolated monolayer WS_2 and a MoS_2/WS_2 heterostructure. The isolated MoS_2 and WS_2 monolayer show strong PL at 1.93 eV and 2.06 eV, respectively, corresponding to their A-exciton resonances. Both exciton PL signals are strongly quenched in the MoS_2/WS_2 heterostructure, suggesting an efficient charge transfer process exists in the heterostructure.

4.3.3 Transient absorption measurement

To directly probe the charge transfer process and its ultrafast dynamics, we measured transient absorption spectra of MoS_2/WS_2 heterostructures using resonant pump-probe spectroscopy. A femtosecond pulse first excites the heterostructure, and the photo-induced changes in the reflection spectrum ($\Delta R/R$) are probed by a laser-generated supercontinuum light after controlled time delays. For atomically thin heterostructures on a transparent sapphire substrate, the reflection change $\Delta R/R$ is directly proportional to the change in absorption coefficient. MoS_2 and WS_2 monolayers have distinctly different exciton transitions. Therefore we can selectively excite the MoS_2 or WS_2 layer using specific resonant optical excitations, and probe the accumulation of electrons and holes in different layers through photo-induced changes in their respective exciton transitions. Specifically, we choose a pump photon energy at 1.86 eV to excite exclusively the A-exciton transition of MoS_2. This pump cannot excite WS_2 directly because the photon energy is far below the absorption threshold of WS_2. Afterwards we examine the photoinduced changes of both WS_2 and MoS_2 exciton resonances in transient absorption spectra from 2.0-2.5 eV to probe the charge distribution in heterostructures.

Using a pump fluence of $85\ \mu J/cm^2$, A-excitons in MoS_2 with a density ~ $5\times10^{12}/cm^2$ are generated immediately after photo-excitation. Figure 4.4a shows a two-dimensional plot of transient absorption spectra in a MoS_2/WS_2 heterostructure at 77 K, where the colour scale, the horizontal axis, and the vertical axis represent the magnitude of -ΔR/R, the probe photon energy, and pump-probe time delay, respectively. The figure shows prominent resonant features in transient absorption centred on 2.06 eV and 2.46 eV, with the higher energy feature several times weaker than the lower energy one. Comparing with linear absorption spectra of isolated WS_2 and MoS_2 monolayers (Figure 4.4e), we can attribute these two resonant features respectively to the A and B-exciton transitions in WS_2, although the WS_2 layer is not excited by the pump. To better understand the transient absorption spectra in MoS_2/WS_2 heterostructures, we also performed control experiments for isolated WS_2 and MoS_2 monolayers. In bare WS_2 monolayers no pump-induced signal can be observed above the noise level, consistent with the fact that no direct absorption can take place in WS_2. In isolated MoS_2 monolayers, pump-induced absorption changes in our spectral range is centred at 2.11 eV (Figure 4.4b), corresponding to the B-exciton transition of MoS_2. Figure 4.4c-d show detailed comparisons of transient absorption spectra in a MoS_2/WS_2 heterostructure and an isolated MoS_2 monolayer at the pump-probe time delay of 1 picosecond (ps) (Figure 4.4c) and 20 ps (Figure 4.4d). Although the resonant features at 2.06 eV for the heterostructure and at 2.11 eV for monolayer MoS_2 are close in energy, they are clearly distinguishable and match well with the A-exciton in WS_2 and B-exciton in MoS_2 in the absorption spectra (Figure 4.4e), respectively. In addition, the transient absorption signal at the WS_2 A-exciton transition in the heterostructure is stronger in magnitude and has a narrower spectral width and a slower decay time constant.

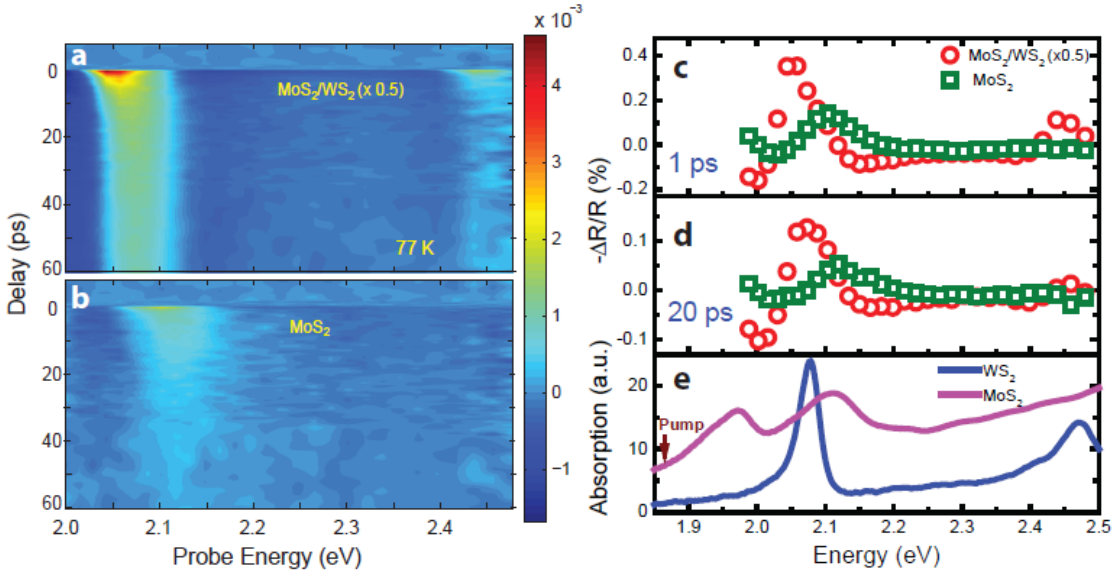

Figure 4.4 Transient absorption spectra of MoS_2/WS_2 heterostructures. a. and **b.** Two-dimensional plots of transient absorption spectra at 77 K from a MoS_2/WS_2 heterostructure (**a**) and an isolated MoS_2 monolayer (**b**) upon excitation of the MoS_2 A-exciton transitions. The horizontal axis, vertical axis, and colour scale represent the probe photon energy, pump-probe time delay, and the transient absorption signal, respectively. Positive signals indicate a pump-induced decrease in absorption. **c.** and **d.** Transient absorption spectra for MoS_2/WS_2 (red circles) and MoS_2 (green square) at 1 ps and 20 ps pump-probe delay, respectively. **e.** Linear absorption spectra of monolayers of MoS_2 (magenta line) and WS_2 (blue line). Although only MoS_2 A-exciton transitions are optically excited, transient absorption spectra in the MoS_2/WS_2 heterostructure are dominated by a resonance feature (red circles in c and d) corresponding to the WS_2 A-exciton transition (blue line in e), which is clearly distinguishable from the resonance feature corresponding to the MoS_2 B-exciton transition in an isolated MoS_2 monolayer (green squares in c and d and magenta line in e). It demonstrates unambiguously an efficient hole transfer from the photoexcited MoS_2 layer to the WS_2 layer in MoS_2/WS_2 heterostructures.

Our transient absorption measurements of MoS_2/WS_2 heterostructures establish unambiguously that optical excitation in MoS_2 leads to strong modification of exciton transitions in WS_2, which has a larger optical bandgap. It provides direct evidence of efficient charge separation in photo-excited MoS_2/WS_2 heterostructures as described in Figure 4.1: electron hole

pairs are initially created in the MoS_2 layer, but holes quickly transfer to the WS_2 layer due to the type-II band alignment, while electrons stay in the MoS_2 layer. The photo-excited electrons in MoS_2 and holes in WS_2 lead to strong transient absorption signal for exciton transitions in both MoS_2 and WS_2. Transient absorption signals are the strongest for the A-excitons due to their sharper resonances and efficient photo-bleaching effects from Pauli blocking, but B-exciton transitions are also affected. Consequently, the transient absorption spectra in MoS_2/WS_2 heterostructures are dominated by the A-exciton transition in WS_2. Photo-induced changes of B-exciton transitions in the MoS_2/WS_2 heterostructure (Figure 4.4a) and in the MoS_2 monolayer (Figure 4.4b) can also be identified, but they are significantly weaker than that of A-exciton transitions. Room temperature data show similar.

4.3.4 Determination of charge transfer time

The rise time of the WS_2 A-exciton transient absorption signal probes directly the hole transfer dynamics from the MoS_2 layer because this signal exists only after the hole transfer, but not right at the excitation of MoS_2. Figure 4.5 shows the dynamic evolution of the WS_2 A-exciton resonance in the MoS_2/WS_2 heterostructure (Figure 4.5a), which can be compared to the transient absorption signal for the B-exciton resonance in an isolated MoS_2 monolayer (Figure 4.5b). We found that the rise time in both signals are almost identical, and it is limited by the laser pulse duration ~ 250 fs. In Figure 4b the MoS_2 monolayer is directly pumped, and the photo-induced signal should appear instantaneously. (The rise time of pump-induced A exciton and B exciton signals in MoS_2 has indistinguishable behavior.) We could reproduce the ultrafast dynamics in the MoS2 monolayer in Figure 4.5b by convoluting the instrument response function (the blue dashed curve in Figure 4.5b) with an instantaneous response in MoS_2. Using the same instrument response function for time convolution, we can then reproduce the experimentally observed signal in the

heterostructure with a rise time shorter than 50 fs (red line in Figure 4.5a). Therefore our results show that holes are transferred from the MoS_2 layer to the WS_2 layer within 50 fs after optical excitation of the MoS_2/WS_2 heterostructure, a remarkably fast rate. Similar ultrafast hole transfer also happens at room temperature. This hole transfer time is much shorter than the exciton lifetime and most other dynamics processes in MX_2 monolayers, which are on the order of several to tens of picosecond. Electrons and holes can therefore be efficiently separated into different layers immediately after their generation. Consequently, PL from MoS_2 and WS_2 exciton resonances will be strongly quenched, as we observed previously.

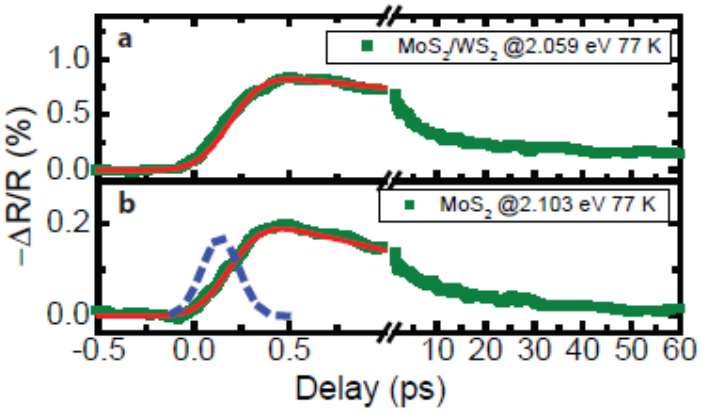

Figure 4.5 Ultrafast hole transfer dynamics from vertical cuts in Figure 4.4a and 4.4b. a. The evolution of transient absorption signals at the WS_2 A-exciton resonance in the MoS_2/WS_2 heterostructure. **b.** The dynamic evolution of transient absorption signals at the MoS_2 B-exciton resonance in the isolated MoS_2 monolayer. Both signals show almost identical ultrafast rise time, which is limited by the laser pulse duration ~ 250 fs. By convoluting the instrument response function (blue dashed line in b) and an instantaneous response in MoS_2, we can reproduce the ultrafast dynamics in the MoS_2 monolayer (red trace in b). Similar convolution shows that the rise time in MoS_2/WS_2 monolayer is around 25 fs (red trace in a), and has an upper limit of 50 fs. It demonstrates that holes can transfer from the photoexcited MoS_2 layer to the WS_2 layer within 50 fs in the MoS_2/WS_2 heterostructure.

4.3.5 Effect of Coulomb interaction and lattice mismatch on charge transfer dynamics

Our experimental data establishes that charge separation in MoS_2/WS_2 heterostructures is very efficient, although the band offset between MoS_2 and WS_2 is smaller than the predicted exciton binding energy in monolayer MX_2. Energetically uncorrelated free electrons and holes in separated MoS_2 and WS_2 layers cannot be produced through the excitation of MoS_2 A-excitons. However, the MoS_2 and WS_2 layers are only ~0.62 nm separated from each other[72], suggesting that even for layer-separated electrons and holes, strong Coulomb interactions can lead to bound exciton states. These exciton states with electron and hole residing in different layers can be energetically favourable compared to an exciton confined to only MoS_2 layer, and are likely to be responsible for the efficient charge separation observed in MoS_2/WS_2 heterostructures. Such bounded excitons with electron and hole in different materials, known as charge transfer excitons (CTC), have also been investigated in other type-II heterojunctions, such as molecular donor/acceptor interfaces in the context of organic photovoltaics[77, 78, 86].

The observed sub-50 fs hole transfer time is remarkably short considering that the MoS_2 and WS_2 layers are twisted relative to each other and are coupled by relatively weak van der Waals interactions. One factor contributing to the ultrafast charge transfer rate in atomically thin heterostructures is the close proximity of the two heterolayers, because electrons or holes only need to move less than 1 nm vertically for the charge transfer process to happen. Still, the 50 fs hole transfer time for van der Waals heterostructures is fast. Microscopic understanding of this ultrafast hole transfer in MX_2 heterostructures requires detailed theoretical studies to examine the hybridization of electronic states in twisted heterolayers and the dynamic evolution of photo-excited states due to electron-phonon and electron-electron interactions. For example, because

MoS_2/WS_2 heterostructures are extended crystalline 2D layers, resonant charge transfer has to satisfy both energy and momentum conservations, and electronic coupling between states with different momenta in the Brillouin zone can vary significantly. It is known that for MoS_2 bilayers, electronic coupling at the K point in the Brillouin zone is weak. Electron wavefunction hybridization at the Γ point, however, is much stronger, which leads to a rise in Γ point valence band and an indirect bandgap in bilayer MoS_2.[6, 7] Electronic coupling between incommensurate MoS_2 and WS_2 can play an important role in the charge transfer dynamics of twisted MoS_2/WS_2 heterostructures, the behaviour of which has been little studied so far. Because van der Waals heterostructures have atomically sharp interfaces with no dangling bonds and well-defined optical resonances, they provide an ideal model system for further experimental and theoretical investigations of interfacial charge transfer processes and the charge transfer exciton states.

The ultrafast charge transfer process in atomically thin MX_2 heterostructures has important implications for photonic and optoelectronic applications. MX_2 semiconductors have extremely strong optical absorption, and has been considered previously for photodetectors[69], photovoltaics[87] and photocatalysis[88]. Compared with organic photovoltaic materials, these 2D layers have crystalline structure and better electrical transport properties. Our studies here show that the type-II MX_2 heterostructures also exhibit femtosecond charge transfer rate, which provides an ideal way to spatially separate electrons and holes for electrical collection and utilization.

4.4 Conclusions and outlook

In summary, I have demonstrated for the first time efficient charge transfer in MoS_2/WS_2 heterostructures through combined PL mapping and transient absorption measurement. We

quantitatively determine the ultrafast hole transfer time to be less than 50 fs. Our study suggests that MX_2 heterostructures, with their remarkable electrical and optical properties and rapid development of large area synthesis, hold great promise for future optoelectronic and photovoltaic applications.

Bibliography

1. Geim, A.K. and K.S. Novoselov, *The rise of graphene.* Nat Mater, 2007. **6**(3): p. 183-191.
2. Geim, A.K. and I.V. Grigorieva, *Van der Waals heterostructures.* Nature, 2013. **499**(7459): p. 419-425.
3. Mak, K.F., et al., *Optical spectroscopy of graphene: From the far infrared to the ultraviolet.* Solid State Communications, 2012. **152**(15): p. 1341-1349.
4. Wang, F., et al., *Gate-Variable Optical Transitions in Graphene.* Science, 2008. **320**(5873): p. 206-209.
5. Horng, J., et al., *Drude conductivity of Dirac fermions in graphene.* Physical Review B, 2011. **83**(16): p. 165113.
6. Splendiani, A., et al., *Emerging Photoluminescence in Monolayer MoS2.* Nano Letters, 2010. **10**(4): p. 1271-1275.
7. Mak, K.F., et al., *Atomically thin MoS 2: a new direct-gap semiconductor.* Physical Review Letters, 2010. **105**(13): p. 136805.
8. Xiao, D., et al., *Coupled Spin and Valley Physics in Monolayers of MoS2 and Other Group-VI Dichalcogenides.* Physical Review Letters, 2012. **108**(19).
9. Chernikov, A., et al., *Exciton Binding Energy and Nonhydrogenic Rydberg Series in Monolayer ${\mathrm{WS}}_{2}$.* Physical Review Letters, 2014. **113**(7): p. 076802.
10. Ye, Z., et al., *Probing excitonic dark states in single-layer tungsten disulphide.* Nature, 2014. **513**(7517): p. 214-218.
11. Ugeda, M.M., et al., *Giant bandgap renormalization and excitonic effects in a monolayer transition metal dichalcogenide semiconductor.* Nat Mater, 2014. **13**(12): p. 1091-1095.

12. Gunawan, O., et al., *Valley Susceptibility of an Interacting Two-Dimensional Electron System.* Physical Review Letters, 2006. **97**(18): p. 186404.

13. Nair, R.R., et al., *Fine Structure Constant Defines Visual Transparency of Graphene.* Science, 2008. **320**(5881): p. 1308.

14. Mak, K.F., et al., *Measurement of the Optical Conductivity of Graphene.* Physical Review Letters, 2008. **101**(19): p. 196405.

15. Li, Z.Q., et al., *Dirac charge dynamics in graphene by infrared spectroscopy.* Nat Phys, 2008. **4**(7): p. 532-535.

16. Schuller, J.A., et al., *Plasmonics for extreme light concentration and manipulation.* Nat Mater, 2010. **9**(3): p. 193-204.

17. Mühlschlegel, P., et al., *Resonant Optical Antennas.* Science, 2005. **308**(5728): p. 1607-1609.

18. Lezec, H.J., J.A. Dionne, and H.A. Atwater, *Negative Refraction at Visible Frequencies.* Science, 2007. **316**(5823): p. 430-432.

19. Valentine, J., et al., *Three-dimensional optical metamaterial with a negative refractive index.* Nature, 2008. **455**(7211): p. 376-379.

20. Chen, H.-T., et al., *Active terahertz metamaterial devices.* Nature, 2006. **444**(7119): p. 597-600.

21. Chen, H.-T., et al., *A metamaterial solid-state terahertz phase modulator.* Nat Photon, 2009. **3**(3): p. 148-151.

22. Chen, H.-T., et al., *Electronic control of extraordinaryterahertz transmission throughsubwavelength metal hole arrays.* Opt. Express, 2008. **16**(11): p. 7641-7648.

23. Yu, P.Y. and M. Cardona, *Fundamentals of Semiconductors.* 2004: p. p. 305.

24. Novoselov, K.S., et al., *Two-dimensional gas of massless Dirac fermions in graphene.* Nature, 2005. **438**(7065): p. 197-200.

25. Zhang, Y., et al., *Experimental observation of the quantum Hall effect and Berry's phase in graphene.* Nature, 2005. **438**(7065): p. 201-204.

26. Papasimakis, N., et al., *Graphene in a photonic metamaterial.* Opt. Express, 2010. **18**(8): p. 8353-8359.

27. Liu, M., et al., *A graphene-based broadband optical modulator.* Nature, 2011. **474**(7349): p. 64-67.

28. Xia, F., et al., *Ultrafast graphene photodetector.* Nat Nano, 2009. **4**(12): p. 839-843.

29. Ju, L., et al., *Graphene plasmonics for tunable terahertz metamaterials.* Nat Nano, 2011. **6**(10): p. 630-634.

30. Yan, H., et al., *Tunable infrared plasmonic devices using graphene/insulator stacks.* Nat Nano, 2012. **7**(5): p. 330-334.

31. Fei, Z., et al., *Gate-tuning of graphene plasmons revealed by infrared nano-imaging.* ArXiv:1202.4993v2, 2012.

32. Echtermeyer, T.J., et al., *Strong plasmonic enhancement of photovoltage in graphene.* Nat Commun, 2011. **2**: p. 458.

33. Liu, Y., et al., *Plasmon resonance enhanced multicolour photodetection by graphene.* Nat Commun, 2011. **2**: p. 579.

34. Dawlaty, J.M., et al., *Measurement of the optical absorption spectra of epitaxial graphene from terahertz to visible.* Applied Physics Letters, 2008. **93**(13): p. 131905.

35. Gusynin, V.P., S.G. Sharapov, and J.P. Carbotte, *Sum rules for the optical and Hall conductivity in graphene.* Physical Review B, 2007. **75**(16): p. 165407.

36. Link, S. and M.A. El-Sayed, *Spectral Properties and Relaxation Dynamics of Surface Plasmon Electronic Oscillations in Gold and Silver Nanodots and Nanorods.* The Journal of Physical Chemistry B, 1999. **103**(40): p. 8410-8426.

37. Kim, K.S., et al., *Large-scale pattern growth of graphene films for stretchable transparent electrodes.* Nature, 2009. **457**(7230): p. 706-710.

38. Li, X., et al., *Large-Area Synthesis of High-Quality and Uniform Graphene Films on Copper Foils.* Science, 2009. **324**(5932): p. 1312-1314.

39. Zou, Y., et al., *Interaction between graphene and metamaterials: split rings vs. wire pairs.* Opt. Express, 2012. **20**(11): p. 12198-12204.

40. Noda, S., M. Fujita, and T. Asano, *Spontaneous-emission control by photonic crystals and nanocavities.* Nat Photon, 2007. **1**(8): p. 449-458.

41. Faraon, A., et al., *Fast Electrical Control of a Quantum Dot Strongly Coupled to a Photonic-Crystal Cavity.* Physical Review Letters, 2010. **104**(4): p. 047402.

42. Sukang, B., et al., *30-Inch Roll-Based Production of High-Quality Graphene Films for Flexible Transparent Electrodes.* CORD Conference Proceedings, 2009.

43. Xu, X., et al., *Spin and pseudospins in layered transition metal dichalcogenides.* Nat Phys, 2014. **10**: p. 343.

44. Wang, Q.H., et al., *Electronics and optoelectronics of two-dimensional transition metal dichalcogenides.* Nature Nanotechnology, 2012. **7**(11): p. 699-712.

45. Cao, T., et al., *Valley-selective circular dichroism of monolayer molybdenum disulphide.* Nature Communications, 2012. **3**.

46. Mak, K.F., et al., *Control of valley polarization in monolayer MoS2 by optical helicity.* Nature Nanotechnology, 2012. **7**(8): p. 494-498.

47. Zeng, H.L., et al., *Valley polarization in MoS2 monolayers by optical pumping.* Nature Nanotechnology, 2012. **7**(8): p. 490-493.

48. Jones, A.M., et al., *Optical generation of excitonic valley coherence in monolayer WSe2.* Nature Nanotechnology, 2013. **8**(9): p. 634-638.

49. Zhang, Y.J., et al., *Electrically Switchable Chiral Light-Emitting Transistor.* Science, 2014. **344**(6185): p. 725-728.

50. Mak, K.F., et al., *The valley Hall effect in MoS2 transistors.* Science, 2014. **344**(6191): p. 1489-1492.

51. Poole, C.P., *Electron spin resonance 2nd edn (Wiley, New York, 1983)*

52. Koppens, F.H.L., et al., *Driven coherent oscillations of a single electron spin in a quantum dot.* Nature, 2006. **442**(7104): p. 766-771.

53. Gupta, J.A., et al., *Ultrafast manipulation of electron spin coherence.* Science, 2001. **292**(5526): p. 2458-2461.

54. Press, D., et al., *Complete quantum control of a single quantum dot spin using ultrafast optical pulses.* Nature, 2008. **456**(7219): p. 218-221.

55. Shi, H., et al., *Exciton Dynamics in Suspended Monolayer and Few-Layer MoS2 2D Crystals.* ACS Nano, 2012. **7**(2): p. 1072-1080.

56. Wang, Q., et al., *Valley Carrier Dynamics in Monolayer Molybdenum Disulfide from Helicity-Resolved Ultrafast Pump–Probe Spectroscopy.* ACS Nano, 2013. **7**(12): p. 11087-11093.

57. Sie, E.J., et al., *Biexciton formation in monolayer MoS2 observed by transient absorption spectroscopy.* arXiv preprint arXiv:1312.2918, 2013.

58. Mak, K.F., et al., *Measurement of the Optical Conductivity of Graphene.* Physical Review Letters, 2008. **101**(19).

59. Cohentannoudji, C. and S. Reynaud, *Dressed-atom description of resonance fluorescence and absorption-spectra of a multilevel atom in an intense laser-beam.* Journal of Physics B-Atomic Molecular and Optical Physics, 1977. **10**(3): p. 345-363.

60. Shen, Y.-R., *The principles of nonlinear optics.* New York, Wiley-Interscience, 1984, 1984. **1**.

61. Von Lehmen, A., et al., *Optical Stark effect on excitons in GaAs quantum wells.* Optics Letters, 1986. **11**(10): p. 609-611.

62. Rostami, H., A.G. Moghaddam, and R. Asgari, *Effective lattice Hamiltonian for monolayer MoS2: Tailoring electronic structure with perpendicular electric and magnetic fields.* Physical Review B, 2013. **88**(8).

63. Shi, H.L., et al., *Quasiparticle band structures and optical properties of strained monolayer MoS2 and WS2.* Physical Review B, 2013. **87**(15).

64. Ponomarenko, L.A., et al., *Cloning of Dirac fermions in graphene superlattices.* Nature, 2013. **497**(7451): p. 594-597.

65. Hunt, B., et al., *Massive Dirac Fermions and Hofstadter Butterfly in a van der Waals Heterostructure.* Science, 2013. **340**(6139): p. 1427-1430.

66. Dean, C.R., et al., *Hofstadter/'s butterfly and the fractal quantum Hall effect in moire superlattices.* Nature, 2013. **497**(7451): p. 598-602.

67. Britnell, L., et al., *Field-Effect Tunneling Transistor Based on Vertical Graphene Heterostructures.* Science, 2012. **335**(6071): p. 947-950.

68. Sup Choi, M., et al., *Controlled charge trapping by molybdenum disulphide and graphene in ultrathin heterostructured memory devices.* Nat Commun, 2013. **4**: p. 1624.

69. Britnell, L., et al., *Strong Light-Matter Interactions in Heterostructures of Atomically Thin Films.* Science, 2013. **340**(6138): p. 1311-1314.

70. Lopez-Sanchez, O., et al., *Ultrasensitive photodetectors based on monolayer MoS2.* Nat Nano, 2013. **8**(7): p. 497-501.

71. Gong, C., et al., *Band alignment of two-dimensional transition metal dichalcogenides: Application in tunnel field effect transistors.* Applied Physics Letters, 2013. **103**(5): p. 053513.

72. Komsa, H.-P. and A.V. Krasheninnikov, *Electronic structures and optical properties of realistic transition metal dichalcogenide heterostructures from first principles.* Physical Review B, 2013. **88**(8): p. 085318.

73. Kang, J., et al., *Band offsets and heterostructures of two-dimensional semiconductors.* Applied Physics Letters, 2013. **102**(1): p. 012111.

74. Terrones, H., F. López-Urías, and M. Terrones, *Novel hetero-layered materials with tunable direct band gaps by sandwiching different metal disulfides and diselenides.* Sci. Rep., 2013. **3**.

75. Berkelbach, T.C., M.S. Hybertsen, and D.R. Reichman, *Theory of neutral and charged excitons in monolayer transition metal dichalcogenides.* Physical Review B, 2013. **88**(4): p. 045318.

76. Qiu, D.Y., F.H. da Jornada, and S.G. Louie, *Optical Spectrum of ${\mathrm{MoS}}_{2}$: Many-Body Effects and Diversity of Exciton States.* Physical Review Letters, 2013. **111**(21): p. 216805.

77. Grancini, G., et al., *Hot exciton dissociation in polymer solar cells.* Nat Mater, 2013. **12**(1): p. 29-33.

78. Jailaubekov, A.E., et al., *Hot charge-transfer excitons set the time limit for charge separation at donor/acceptor interfaces in organic photovoltaics.* Nat Mater, 2013. **12**(1): p. 66-73.

79. Kaake, L.G., D. Moses, and A.J. Heeger, *Coherence and uncertainty in nanostructured organic photovoltaics.* The Journal of Physical Chemistry Letters, 2013. **4**(14): p. 2264-2268.

80. van der Zande, A.M., et al., *Grains and grain boundaries in highly crystalline monolayer molybdenum disulphide.* Nature materials, 2013. **12**(6): p. 554-561.

81. Zhang, Y., et al., *Controlled growth of high-quality monolayer WS2 layers on sapphire and imaging its grain boundary.* ACS nano, 2013. **7**(10): p. 8963-8971.

82. Lee, C., et al., *Anomalous lattice vibrations of single-and few-layer MoS2.* ACS nano, 2010. **4**(5): p. 2695-2700.

83. Berkdemir, A., et al., *Identification of individual and few layers of WS2 using Raman Spectroscopy.* Scientific reports, 2013. **3**.

84. Luo, X., et al., *Effects of lower symmetry and dimensionality on Raman spectra in two-dimensional WSe 2.* Physical Review B, 2013. **88**(19): p. 195313.

85. Terrones, H., et al., *New first order Raman-active modes in few layered transition metal dichalcogenides.* Scientific reports, 2014. **4**.

86. Gélinas, S., et al., *Ultrafast long-range charge separation in organic semiconductor photovoltaic diodes.* Science, 2014. **343**(6170): p. 512-516.

87. Gourmelon, E., et al., *MS 2 (M= W, Mo) photosensitive thin films for solar cells.* Solar Energy Materials and Solar Cells, 1997. **46**(2): p. 115-121.

88. Ho, W., et al., *Preparation and photocatalytic behavior of MoS2 and WS2 nanocluster sensitized TiO2.* Langmuir, 2004. **20**(14): p. 5865-5869.